

## Accepted Manuscript

Interseismic crustal deformation in the Taiwan plate boundary zone revealed by GPS observations, seismicity, and earthquake focal mechanisms

Ya-Ju Hsu, Shui-Beih Yu, Mark Simons, Long-Chen Kuo, Horng-Yue Chen

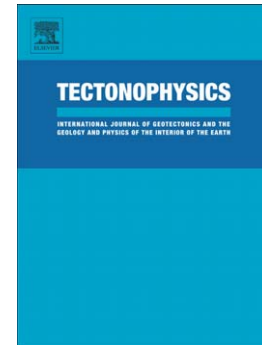
PII: S0040-1951(08)00577-5  
DOI: doi: [10.1016/j.tecto.2008.11.016](https://doi.org/10.1016/j.tecto.2008.11.016)  
Reference: TECTO 124415

To appear in: *Tectonophysics*

Received date: 29 May 2008  
Revised date: 11 November 2008  
Accepted date: 18 November 2008

Please cite this article as: Hsu, Ya-Ju, Yu, Shui-Beih, Simons, Mark, Kuo, Long-Chen, Chen, Horng-Yue, Interseismic crustal deformation in the Taiwan plate boundary zone revealed by GPS observations, seismicity, and earthquake focal mechanisms, *Tectonophysics* (2008), doi: [10.1016/j.tecto.2008.11.016](https://doi.org/10.1016/j.tecto.2008.11.016)

This is a PDF file of an unedited manuscript that has been accepted for publication. As a service to our customers we are providing this early version of the manuscript. The manuscript will undergo copyediting, typesetting, and review of the resulting proof before it is published in its final form. Please note that during the production process errors may be discovered which could affect the content, and all legal disclaimers that apply to the journal pertain.



1 **Interseismic crustal deformation in the Taiwan plate boundary zone revealed by**  
2 **GPS observations, seismicity, and earthquake focal mechanisms**

3 Ya-Ju Hsu<sup>1</sup>, Shui-Beih Yu<sup>1</sup>, Mark Simons<sup>2</sup>, Long-Chen Kuo<sup>1</sup>, and Horng-Yue Chen<sup>1</sup>

4 1. Institute of Earth Sciences, Academia Sinica, P.O. Box 1-55, Nankang, Taipei, Taiwan

5 Tel: 886-2-27839910 ext.415 / Fax: 886-2-27883493/

6 e-mail: [yaru@earth.sinica.edu.tw](mailto:yaru@earth.sinica.edu.tw)

7 2. Division of Geological and Planetary Sciences, California Institute of Technology, Pasadena, CA  
8 91125, USA.

ACCEPTED MANUSCRIPT

9 **Abstract**

10 We use GPS-derived surface velocities, seismicity, as well as estimates of earthquake focal  
11 mechanisms from the time period before the 1999 Chi-Chi earthquake to evaluate spatial variations of  
12 surface strain rate and crustal stress regime in the Taiwan plate boundary zone. We estimate strain rates  
13 with a new but simple approach that solves for surface velocity on a rectangular grid while accounting  
14 for the distance between observations and each grid node and the impact of a spatially variable density  
15 of observations. This approach provides stable and interpretable strain-rate estimates. In addition, we  
16 perform a stress tensor inversion using earthquake focal mechanisms determined by P waves  
17 first-motion polarities. Our estimates of the principal orientations of two-dimensional surface strain rate  
18 tensor generally agree with the inferred orientations of the stress axes. This agreement suggests that a  
19 large scale variation of stress orientations from the surface to the base of the crust is insignificant and  
20 the predicted faulting style is consistent with stress buildup during the interseismic loading. We find  
21 that the geometric configuration of the Chinese continental margin alone can not fully explain the  
22 distribution of maximum contraction and compressive axes in Taiwan. Distribution of seismicity and  
23 focal mechanisms before and after the Chi-Chi mainshock suggest that the maximum principal stress  
24 axis is vertically-oriented in the Central Range; in contrast to the horizontal maximum principal stress  
25 axis in western Taiwan and the Longitudinal Valley. Extension in the Central Range reflects the  
26 consequence of exhumation and crustal thickening.

## 27 1. Introduction

28 The island of Taiwan is located in the plate boundary zone between the Eurasian (EUP) and  
29 Philippine Sea plates (PHP) and is bound by two subduction zones. In the north, the PHP subducts  
30 beneath the Ryukyu Arc; while to the south, the South China Sea block of the EUP subducts beneath  
31 the PHP (Fig. 1). The Taiwan orogeny results from the collision of the Luzon volcanic arc in the PHP  
32 and the Chinese continental margin in the EUP beginning about 3-6 Ma ago (Suppe, 1984; Barrier and  
33 Angelier, 1986; Teng, 1996; Huang *et al.*, 1997). The plate convergence rate across the Island is about  
34 8 cm/yr in a direction of N310°E (Seno *et al.*, 1993; Yu *et al.*, 1997).

35 Taiwan can be divided into six northeast-trending physiographic regions which are separated by  
36 major faults (Fig. 1). These regions are, from west to east, the Coastal Plain, the Western Foothills, the  
37 Hsueshan Range, the Central Range, the Longitudinal Valley, and the Coastal Range. The Coastal Plain  
38 is composed of Quaternary alluvial deposits derived from the Western Foothills and the Central Range.  
39 The Western Foothills consists of a thick sequence of shallow marine to shelf sediments from the late  
40 Oligocene, Miocene, to early Pleistocene. The Hsueshan Range is mostly composed of Eocene and  
41 Oligocene sediments. The Central Range is characterized by Tertiary metamorphism, in contrast with  
42 the adjacent non-metamorphic rocks in the Western Foothills. The 150 km long NNE-trending  
43 Longitudinal Valley separates the Central Range to the west and the Coastal Range to the east.  
44 Quaternary clastic fluvial sediments fill this valley. The Coastal Range is composed of Neogene  
45 andesitic volcanic rocks of the northern Luzon Arc. The Longitudinal Valley Fault (LVF) runs more or

46 less along the western margin of the Coastal Range and it is a major active structure in eastern Taiwan  
47 (Biq, 1972; Hsu, 1976; Wu, 1978; Barrier and Angelier, 1986; Ho, 1986).

48 An island-wide GPS network composed of more than 195 campaign-mode sites and 17 continuous  
49 stations have been established by the Institute of Earth Sciences, Academia Sinica, Ministry of the  
50 Interior (MOI) and other institutions since 1989. Most of the campaign-mode sites have been occupied  
51 at least once annually since 1990. The first velocity field in the Taiwan area was estimated from the  
52 1990-1995 GPS observations by Yu et al. (1997). The convergence across the Taiwan arc-continent  
53 collision zone inferred from GPS velocity field is about 80 mm/yr in the northwest direction. The  
54 crustal strain is accumulated in two major zones: the fold-and-thrust belt in the Western Foothills, and  
55 the Longitudinal Valley as well as the Coastal Range in eastern Taiwan.

56 On 21 September 1999, the  $M_w$  7.6 devastating Chi-Chi earthquake struck central Taiwan. The  
57 Chi-Chi earthquake resulted from the reactivation of the Chelungpu Fault (CLPF), a major frontal  
58 thrust within the Western Foothills (Fig. 2). Most of the GPS sites were affected by this large event and  
59 showed significant coseismic movements.

60 For studying the interseismic deformation before the 1999 Chi-Chi earthquake, we derive an  
61 updated Taiwan velocity field using all available campaign-mode and continuous GPS data collected  
62 between 1993 and 1999. We use this velocity field sampled at irregular points to estimate velocities  
63 sampled on an arbitrarily fine regular rectangular grid. To obtain a continuous strain-rate field, we  
64 compute strain rates from gradients of interpolated velocities. The details of methods are presented in a

65 later section after describing the input GPS-derived velocity observations. We then compare principal  
66 strain-rate axes with stress axes derived from earthquake focal mechanisms and discuss their  
67 implications. In addition, we provide new insights into the crustal stress field in the Taiwan region.

68 Previous studies based on fault slip data (Angelier *et al.*, 1986), earthquake focal mechanisms  
69 (Yeh *et al.*, 1991), borehole breakout data (Suppe *et al.*, 1985) as well as GPS data (Bos *et al.*, 2003;  
70 Chang *et al.*, 2003) demonstrate a fan-shaped pattern of maximum compressive or contraction axes in  
71 Taiwan. This feature is believed to be affected by the shape of the Chinese continental margin (Hu *et al.*,  
72 1996). However, our study shows the correlation between the trends of the maximum contraction or  
73 compressive axes and the shape of the Chinese continental margin is not perfect. Furthermore, we find  
74 the lateral extrusion in SW Taiwan may not fully explain the sharp variations of strain-rate and stress  
75 axes between SW Taiwan and the southern Central Range. The tectonic escape in SW Taiwan is  
76 previously inferred from sandbox experiments (Lu and Malavieille, 1994). Data sets based on  
77 geological, geodetic and seismological evidences also support this hypothesis (Lu and Malavieille,  
78 1994; Lacombe *et al.*, 2001; Bos *et al.*, 2003; Gourley, 2006; Gourley *et al.*, 2007; Hu *et al.*, 2007). The  
79 mechanism of the lateral extrusion is perhaps due to low lateral confining stress offshore SW Taiwan  
80 and the presence of the Peikang basement high as a rigid indenter (Hu *et al.*, 1996). However, direct  
81 onland structural evidence of tectonic extrusion is poor. Based on Quaternary paleostress patterns that  
82 that the lateral extrusion have began recently, during the late Pleistocene (Lacombe *et al.*, 2001). On the  
83 other hand, we discuss the extension in the Central Range that was first inferred by GPS observations

84 (Yu and Chen, 1994) and was later confirmed by structural fabrics (Crespi *et al.*, 1996) and inferences  
85 of the GPS strain-rate field (Bos *et al.*, 2003; Chang *et al.*, 2003). Previous studies suggest that the  
86 extension in the Central Range resulted from crustal exhumation after the subduction of the South  
87 China Sea block (Lin, 2000). The exhumation occurred when the increase of buoyancy forces on the  
88 light subducted continental crust is sufficient to produce decoupling at the base of the crust (Lin, 2000).  
89 Recent work suggests that the extension in northeastern Central Range may be driven by the current  
90 collision between the PHP and the basement high indenter (Gourley *et al.*, 2007); while the extension  
91 in the southern Central Range could be due to the lateral extrusion in SW Taiwan (Gourley, 2006). We  
92 suggest that the extension in the Central Range may be a result of exhumation associated with  
93 overthickened continental crust or the buoyancy force of the subducted continental crust (Lin, 2000).

94

## 95 **2. Velocity field**

96 We use GPS data from between 1993 and 1999 (before the 1999 Chi-Chi earthquake), including  
97 195 campaign-mode sites and 17 continuous stations operated by the Institute of Earth Sciences,  
98 Academia Sinica (IES), Ministry of the Interior (MOI) and other institutions. To minimize the impact  
99 of atmospheric disturbance in the GPS observations at sub-tropical areas, we divide the full GPS  
100 network into several subnets and conduct surveys at each subnet more or less in the same season every  
101 year. The surveys at various subnets can be conducted during different seasons of the year. Most of  
102 campaign-mode sites used in this study were occupied at least 5 times during this period. We processed

103 the campaign-mode and continuous GPS data using the Bernese v.4.2 software (Hugentobler *et al.*,  
104 2001) with precise ephemerides from the International GNSS services (IGS). The entire GPS data sets  
105 are in a consistent reference frame, the International Terrestrial Reference Frame 1997 (ITRF97), by  
106 taking the ITRF97 coordinates and velocities of an IGS core site, TSKB (Tsukuba, Japan) as a  
107 reference station. Yu and Kuo (2001) give a more detailed description of the procedures for our GPS  
108 data acquisition and processing. The normal equations of single-session solutions for a campaign are  
109 first combined to create a campaign solution. An annual survey campaign for a specific area usually  
110 spans 10-15 days. The multi-year campaign solutions are then combined to estimate the station  
111 velocities (Fig. 2). Comparing to previous results of GPS observations between 1991 and 1995 (Yu *et*  
112 *al.*, 1997), the GPS data used in this study is more robust due to the improvement of technology by  
113 increasing amount of GPS satellites and using high precision GPS satellite orbits. In addition, more  
114 GPS data coverage in time and space facilitate the detection of subtle signals for crustal deformation.

115 The Taiwan interseismic velocity field derived from 1993-1999 GPS measurements is shown in  
116 Fig. 2 and also given with pertinent data in Table 1. The Paisha, Penghu, continuous GPS station  
117 (S01R), situated on the relatively stable Chinese continental margin, is chosen as the reference site.  
118 With respect to Penghu, the GPS velocity increases from north to south in the Coastal Plain and the  
119 Western Foothills; the maximum rates are mostly less than 5 mm/yr in northern Taiwan, ~25 mm/yr  
120 near central Taiwan, then up to ~40 mm/yr in southern Taiwan. The azimuth of GPS velocity also  
121 rotates counterclockwise from N70°W near Maoli-Taichung, to N120°W near Kaohsiung. It is worth

122 nothing that GPS velocities vary from  $\sim 20$  mm/yr south of Tainan to  $\sim 50$  mm/yr near the Kaohsiung  
123 area along the coast (Fig. 2) and the deviation in velocity azimuth is small (less than  $15^\circ$ ). This feature  
124 may imply the existence of a NE-SW trending shear zone between Tainan and Kaohsiung. In eastern  
125 Taiwan, the accumulated crustal strain is mainly accommodated in the NNE trending LVF, bounded by  
126 the Longitudinal Valley and the Coastal Range. The velocity in the eastern side of the LVF, the Coastal  
127 Range, is 26-68 mm/yr in the direction of  $\sim N50^\circ W$  whereas that in the western side of the LVF  
128 decreases to 18-35 mm/yr in the direction of  $\sim N70^\circ W$ . The velocity discontinuity across the LVF is  
129 about 30 mm/yr. The crustal strain in this region is mainly taken up by aseismic slip, especially near the  
130 surface, and earthquakes at greater depths (Yu and Kuo, 2001). In the Ilan plain of northeastern Taiwan,  
131 the velocity vectors trend to the southeast with rates of 8-38 mm/yr. This direction is remarkably  
132 different from other regions in Taiwan.

133

### 134 3. Method to estimate strain-rate field

135 In order to obtain a continuous strain-rate field that ensures compatibility, we first estimate a  
136 spatially continuous surface velocity field. We adopt a  $0.125^\circ \times 0.125^\circ$  grid extending from  $120^\circ E$  to  
137  $122.25^\circ E$  and  $22^\circ N$  to  $25.25^\circ N$ . We then estimate the east and north components of horizontal velocities  
138 at each node using 212 observed GPS horizontal velocities. The contribution of any given observation

139 is weighted as a function that decays with increasing distance from the estimation point (Shen *et al.*,  
 140 1996; Ward, 1998 ). The estimation equation can be written as:

$$141 \begin{bmatrix} v_e^1 \\ v_e^2 \\ \vdots \\ v_e^i \\ v_n^1 \\ v_n^1 \\ \vdots \\ v_n^i \end{bmatrix} = \begin{bmatrix} \mathbf{O}_{ij} & 0 \\ 0 & \mathbf{O}_{ij} \end{bmatrix} \begin{bmatrix} \hat{v}_e^1 \\ \hat{v}_e^2 \\ \vdots \\ \hat{v}_e^j \\ \hat{v}_n^1 \\ \hat{v}_n^2 \\ \vdots \\ \hat{v}_n^j \end{bmatrix} \quad (1)$$

142 where  $\mathbf{O}_{ij} = \exp(-d_{ij}^2 / D_i^2)$ ;  $v_e^i$  and  $v_n^i$  are east and north components of velocities at the  $i^{\text{th}}$  GPS  
 143 station;  $d_{ij}$  is the distance between the  $i^{\text{th}}$  GPS station and the  $j^{\text{th}}$  node;  $D_i$  is a spatial length and  
 144 controls the size of interpolation window. We search for minimum  $D_i$  at each GPS station to ensure it  
 145 located inside the convex hull composed by nodes (the size of  $D_i$  is about 30~40 km);  $\hat{v}_e^i$  and  $\hat{v}_n^i$  are  
 146 estimated north and east component at the  $j^{\text{th}}$  point. Equation (1) can be written as:

$$147 \mathbf{d} = \mathbf{Gm} \quad (2)$$

148 where  $\mathbf{d}$  is a matrix of observed GPS velocities,  $\mathbf{G}$  is a matrix of Green's functions related to the  
 149 distance between each GPS station and node, and  $\mathbf{m}$  is the desired velocity field. To ensure the velocity  
 150 varies smoothly in space and to balance the representative area associated with individual data points,  
 151 we augment equation (2) to be:

$$152 \quad \begin{bmatrix} \mathbf{W}d \\ 0 \end{bmatrix} = \begin{bmatrix} \mathbf{W}G \\ \alpha \nabla^2 \end{bmatrix} m \quad (3)$$

153 where  $\nabla^2$  is the smoothing matrix using the finite difference approximation of the Laplacian operator;  
 154 and  $\alpha$  serves as the weighting of the model roughness versus data misfit. We choose the value of  $\alpha$   
 155 by cross-validation (Matthews and Segall, 1993). In order to take account the variable contributions  
 156 from individual data, we weighted each observation with two types of weighting, including the  
 157 observational error ( $\mathbf{W}_s$ ) and the station density ( $\mathbf{W}_a$ ), each one equally contributes to the inversion. The  
 158 weighting matrix,  $\mathbf{W}$ , equals to the multiple of  $\mathbf{W}_s$  and  $\mathbf{W}_a$ ; where  $\mathbf{W}_s$  is the reciprocal of observation  
 159 error,  $\mathbf{W}_a$  is estimated from the area of the Voronoi cells associated with the geodetic network. The  
 160 GPS site associated with a given Voronoi cell will be the closest site to any point in that cell. Thus the  
 161 area of cell represents a good metric for the area that a given site should represent. The Voronoi cells  
 162 for our data set are given in Fig. 3a. Voronoi vertices located offshore are replaced by the closest point  
 163 on land (Fig. 3b). In addition, we assign a maximum area weighting for several sites located on  
 164 offshore islands such as Penghu, Luato and Lanhsu. The actual value  $\mathbf{W}_a$  corresponds to the square root  
 165 of cell area associated with a given GPS station. Using  $\mathbf{W}_a$  has the affect of stabilizing the inversion  
 166 and avoids biased information from irregularly station geometry, such that dense pockets of stations do  
 167 not dominate results. The modeling velocity and residuals are shown in Fig. 4a, b. The strain rate at  
 168 each node is determined by taking spatial derivatives of modeling velocities, with fully propagated  
 169 covariance matrix from observed GPS velocities to estimated strain rates (Fig. 4c). Note that the large

170 misfit in modeling velocity in the SW Taiwan and the Longitudinal Valley is possibly associated with  
171 fault creep near the surface (Fig. 4b). The sharp velocity discontinuity corresponding to the fault creep  
172 at shallow depths can not be reproduced in our method.

#### 173 **4. Surface strain rates and crustal stress**

174 Earlier studies (Bos *et al.*, 2003; Chang *et al.*, 2003) adopt different methods to estimate the  
175 strain-rate field in Taiwan using GPS velocity between 1990 and 1995 (Yu *et al.*, 1997). Chang *et al.*  
176 (2003) do not consider the GPS velocity errors and the distribution of GPS stations. Bos *et al.* (2003)  
177 describe the surface deformation in terms of the continuous deformation and discrete movements along  
178 faults; requiring a priori knowledge of fault geometries. To illustrate the relationship between strain rate  
179 and stress in the Taiwan plate boundary zone, we first use the aforementioned method to compute the  
180 strain rate field from GPS data between 1993 and 1999 (Fig. 4c) and then compare principal strain-rate  
181 axes with stress axes derived from stress tensor inversions. The one standard deviation of dilatation rate  
182 is shown in Fig. 4d. The errors are normally around  $0.1 \mu\text{strain/yr}$  over most of Taiwan and no more  
183 than  $0.3 \mu\text{strain/yr}$  at the southern and northern tips. The inferred dilatation rates in most areas are  
184 larger than their errors.

185

#### 186 **4.1 The strain-rate field derived from GPS data**

187 Strain rates computed from GPS velocities indicate SW Taiwan and the Longitudinal Valley in

188 eastern Taiwan are experiencing high NW to W - SE to E contraction with the maximum rates more  
189 than  $1 \mu\text{strain/yr}$  (Fig. 4c). The trends of inferred maximum principal contraction axes in western  
190 Taiwan, from north to south, are  $\sim\text{N}40^\circ\text{W}$  in the Hsinchu area,  $\sim\text{N}70^\circ\text{W}$  in the Taichung area and  
191  $\sim\text{N}80^\circ\text{W}$  in the Tainan-Kaohsiung area. In the Longitudinal Valley of eastern Taiwan, the maximum  
192 contraction axis counterclockwise rotates from  $\text{N}30^\circ\text{W}$  in the Hualien area to  $\text{N}60^\circ\text{W}$  in the Taitung  
193 area. The general trends of contraction axes are consistent with previous results based on different  
194 approaches (Bos *et al.*, 2003; Chang *et al.*, 2003).

195 In contrast to the contraction regime in western Taiwan and the Longitudinal Valley, northeastern  
196 Taiwan and the Central Range show significant extension. The trends of extension axes vary from north  
197 to south: they are NW-SE-directed in the Ilan plain, NE-SW-directed near the middle part of the  
198 Central Range, and NEE-SWW-directed in the southern Central Range. In northeastern Taiwan,  
199 orientations of extension axes show a counterclockwise rotation between offshore Ilan ( $\text{N}40^\circ\text{W}$ ) to  
200 inland area ( $\text{N}70^\circ\text{W}$ ) near  $121.5^\circ\text{E}$ ,  $24.5^\circ\text{N}$ . On the other hand, subtle NE-SW and significant  
201 NEE-SWW directed extensions are derived from our model near the middle ( $\sim 24^\circ\text{N}$ ) and southern  
202 portions ( $22^\circ\text{N}$ - $23.5^\circ\text{N}$ ) of the Central Range, respectively. The first-order pattern of the trend of  
203 extension axes corresponds to the results in previous studies (Bos *et al.*, 2003; Chang *et al.*, 2003).

204

#### 205 **4.2 Principal stress axes derived from stress tensor inversions**

206 The GPS velocities image the surface strain rate, while earthquake focal mechanisms demonstrate

207 the state of stress in the seismogenic crust. In order to tell how strain or stress varies with depth, we  
208 examine the stress regime in the crust using earthquake focal mechanisms with depths less than 30 km.  
209 We use focal mechanism determining by first-motion polarities of P waves from Wu et al. (2008). They  
210 implement a genetic algorithm in a non-linear global search to find the best earthquake focal  
211 mechanism with  $M_L > 4$  between 1991 and 2005. In this study, we only use the data before the Chi-Chi  
212 earthquake (1991-1999.7). Alternatively, we could use the earthquake focal mechanisms determined  
213 from the modeling of waveforms recorded by the Broadband Array in Taiwan for Seismology (BATS);  
214 however, the number of shallow earthquakes (Kao and Jian, 2001) is not sufficient for a stress tensor  
215 inversion.

216 We use the algorithm from Michael (1984; 1987) to find the stress tensor that minimizes the  
217 difference between the shear stress on the fault plane and the fault slip rake. In order to find a  
218 continuous variation of stress orientations in space, we use a moving-window inversion on the  
219  $0.25^\circ$ -spacing grid and include all events within a  $0.5^\circ \times 0.5^\circ$  rectangle centered at the node. We  
220 estimate the stress tensor only when there are at least 10 earthquakes within a given rectangular box  
221 (Fig. 5). The resulting maximum and minimum stress axes projected to the surface are shown in Fig. 6.  
222 The length of stress axis is the largest when the plunge is  $0^\circ$  (horizontal) and is close to 0 when the  
223 plunge is  $90^\circ$  (vertical). While we attempt to use an adequate number of focal mechanisms to constrain  
224 the stress field, we are hampered by a limited understanding of the error in the input focal mechanisms.  
225 To estimate the quality of stress tensor inversion, we use a bootstrap method re-sampling actual focal

226 mechanisms to generate 500 synthetic data sets and then computing the 95% confidence region of  
 227 principal stress axes (Fig. 5). We find the trend of maximum principal stress axis,  $\sigma_1$ , is the most  
 228 reliable axis among three and the plunge is close to horizontal, consistent with the compressive stress  
 229 regime dominant in the Taiwan collision zone. The intermediate and minimum stress axes ( $\sigma_2$  and  $\sigma_3$ )  
 230 vary a lot in most regions. Therefore, we only discuss the trend of stress axis,  $\sigma_1$ , and the maximum  
 231 principal strain-rate axis in the next section.

232 The ratio of principal stress difference  $\phi = \frac{\sigma_2 - \sigma_3}{\sigma_1 - \sigma_3}$  from the stress tensor inversion is shown in  
 233 Fig. 7. If  $\sigma_1 = \sigma_2$ , namely  $\phi = 1$ , the stress status of the crust corresponds to a stress regime transitional to  
 234 normal faulting; while if  $\sigma_2 = \sigma_3$ , namely  $\phi = 0$ , corresponds to a stress regime to thrust faulting. For the  
 235 value of  $\phi$  close to 0 or 1, represents the near-transitional stress regime that requires only minor  
 236 fluctuations in stress magnitude to change from one stress regime to the other.

237

### 238 4.3 Comparison of orientations between strain-rate and stress axes and its implication

239 To illustrate the variation of faulting type from surface to the crust, we compare the trends of  
 240 principal strain rates derived from GPS velocity field and principal stress axes derived from earthquake  
 241 focal mechanisms with depths less than 30 km. In Fig. 6, we find that the orientations of principal  
 242 strain-rate and stress axes generally agree. This implies that a large scale variation of stress orientations  
 243 from the surface to the base of the crust is insignificant. Faulting style is consistent with stress buildup  
 244 resulted from the interseismic loading. The first-order patterns of stress and strain-rate axes at the crust

245 are generally correlated with the plate motion. To further elucidate characteristics of regional structures,  
246 we examine areas with sufficient GPS data and earthquake focal mechanisms to detect more subtle  
247 variations. These variations may result from regional tectonics, the lithosphere flexural stress due to  
248 sediment loading in the continental margin, localized lateral strength contrast associated with material  
249 properties, and lateral strength contrast in response to the fault zone (Zoback, 1992).

250 In western Taiwan, the trends of maximum contraction axes and principal compressive axes (Fig.  
251 6) are consistent with a fan-shaped pattern that has been demonstrated from various data sets (Suppe *et*  
252 *al.*, 1985; Angelier *et al.*, 1986; Yeh *et al.*, 1991; Bos *et al.*, 2003; Chang *et al.*, 2003). The fan-shaped  
253 distribution of maximum contraction and compressive axes are primary influenced by the indenter, the  
254 Peikang High (Meng, 1971), in the Chinese continental margin (Hu *et al.*, 1996). To examine this  
255 hypothesis, we compare the shape of the West Taiwan foreland basin (Fig. 4d) with orientations of  
256 maximum contraction and compressive axes. The Peikang High is located on the western fringe of the  
257 foreland basin (Fig. 4d). Seismic and well data suggest that the West Taiwan foreland basin developed  
258 by orogenic loading and flexure of a rift-type continental margin (Lin and Watts, 2002). We find that  
259 the shape of the foreland is only partially correlated with the trend of maximum contraction or  
260 compressive axes (Figs. 4c,d, and 6); therefore, other explanations different from the shape of the  
261 Chinese continental margin need to be investigated. Lin and Watts (2002) interpreted that the low and  
262 active seismicity on the northern and southern Taiwan foreland basin reflect low and high bending  
263 stress due to the curvature of the foreland basin, respectively. The base (~8 km) of the foreland basin is

264 the greatest near Tainan and Kaohsiung areas. The flexural stress due to sediment loading could induce  
265 margin-normal extensional stress on the loaded continental shelf and margin-normal compression in the  
266 adjacent regions (Stein *et al.*, 1989). Limited by the complex shape of the Chinese continental margin  
267 near Tainan and Kaohsiung (Fig. 4d), we can not find a simple correlation between the shape of the  
268 Chinese continental margin and orientations of stress or strain-rate axes. A numerical model is needed  
269 to further clarify the impact of the sediment loading in the future.

270 In addition, the trends of  $\sigma_1$  and contraction axes in the Coastal Plain and the Western Foothills  
271 between Chiayi and Kaohsiung, are perceptible different by about  $20^\circ\sim 40^\circ$  from those in the southern  
272 Central Range (Fig. 6). Regions near SW Taiwan may be experiencing lateral extrusion (Lu and  
273 Malavieille, 1994; Lacombe *et al.*, 2001; Bos *et al.*, 2003; Gourley, 2006; Gourley *et al.*, 2007; Hu *et*  
274 *al.*, 2007). To what extent this lateral-escape tectonic model explains the rotations of  $\sigma_1$  and contraction  
275 axes remain unclear. The strength of crustal material may be very different in SW Taiwan and the  
276 southern Central Range, and could provide another source for the rotation of compressive or  
277 contraction axes. Earlier studies show that the upper crust of SW Taiwan is composed of the  
278 sedimentary wedge (Lacombe *et al.*, 2001) and the P wave velocity is low comparing to that in adjacent  
279 regions (Kim *et al.*, 2005; Wu *et al.*, 2007). In contrast to Pre-Tertiary metamorphic complex in the  
280 Central Range, the sediments in SW Taiwan are too weak to produce earthquakes at shallow depths  
281 (Fig. 8). In summary, we hypothesize that the sharp variations of strain-rate and stress axes between  
282 SW Taiwan and the southern Central Range could be associated with the tectonic escape in SW Taiwan

283 as well as the lateral strength contrast due to different geological materials.

284 Significant extension in northeastern Taiwan (Ilan plain) and the Central Range is inferred from GPS  
285 velocity field in this study and some previous work (Bos *et al.*, 2003; Chang *et al.*, 2003). The result of  
286 stress tensor inversion in the Ilan plain shows that the  $\sigma_1$  axis and the  $\sigma_3$  axis are vertically- and  
287 horizontally- oriented, respectively (Fig. 5), consistent with a normal-faulting stress regime. The  
288 direction of the tension is consistent with the NW-SE extension derived from GPS velocities. The  
289 extension in the Ilan plain is associated with the opening of Okinawa Trough (Sibuet *et al.*, 1987). In  
290 terms of the extension in the Central Range, it is mainly constrained by GPS velocities due to limited  
291 seismicity in the northern portion of the Central Range. Previous studies proposed different hypothesis  
292 to explain the extension of the Central Range, including the crustal exhumation due to the increase of  
293 buoyancy forces on the light subducted continental crust (Lin, 2000), the current collision between the  
294 PSP and the basement high on the EUP (Gourley *et al.*, 2007) as well as the lateral extrusion in SW  
295 Taiwan (Gourley, 2006). We suggest that the extension in the Central Range may be a result of  
296 exhumation associated with overthickened continental crust and the buoyancy force of the subducted  
297 continental crust (Lin, 2000). The exhumation in the Central Range may be due to gravitational  
298 collapse of the upper most crust. Results from fission track ages (Liu, 1982) inferred that the uplift of  
299 the Central Range has increased rapidly since about 3 Ma ago to an average of 9 mm/yr during the last  
300 0.6 Ma. The crustal thickening corresponding to high topography has been inferred from seismic  
301 tomography studies (Kim *et al.*, 2005; Wu *et al.*, 2007). We expect that a negative density anomaly

302 associated the root of the thickened crust would produce extensional stress and strain, as has been seen  
303 in other orogenies such as the Andes and the Himalayas (Zoback, 1992). Results from the  
304 thermokinematic model of the Taiwan mountain belt suggest that crustal thickening and exhumation are  
305 sustained by underplating beneath the eastern part of the Central Range (Simoes *et al.*, 2007).

306 In eastern Taiwan, the deformation is primary taken up by left-lateral oblique thrust faulting in  
307 LVF (Yu and Kuo, 2001). We find a counterclockwise rotation of  $\sigma_1$  axis from the northern to southern  
308 Longitudinal Valley, a similar pattern is found in strain-rate contraction axes (Fig. 6). The azimuthal  
309 changes of principal compressive axes might be correlated with the change of subduction polarity in  
310 northern and southern Taiwan (Fig. 1, 8).

311

#### 312 **4.4 The crustal stress field derived from seismicity and focal mechanisms**

313 We find most shallow earthquakes are located near the mountain front in western Taiwan (Fig.  
314 8). Previous study in the Himalaya shows that the high topography affect the seismicity distribution  
315 (Bollinger *et al.*, 2004). To evaluate the impact of high topography on the seismicity pattern in Taiwan,  
316 we examine seismicity and earthquake focal mechanisms with  $M_L > 4$  and depth  $< 30$  km (Wu *et al.*,  
317 2008) before and after the Chi-Chi earthquake (Fig. 9). Seismicity near the northeastern CLPF and the  
318 northern portion of eastern Central Range (*A* in Fig. 9b) is quiescent before the Chi-Chi earthquake;  
319 while the seismicity becomes active after the Chi-Chi earthquake (Fig. 9). Many normal-faulting  
320 earthquakes occur in the Central Range after the Chi-Chi mainshock (*A* in Fig. 9b). This feature could

321 be an indication of the rotation of maximum principal stress axis from horizontally- to  
322 vertically-oriented in response to the high topography. The inferred maximum principal stress ( $\sigma_1$ ) in  
323 these regions is close to vertical and the minimum principal stress ( $\sigma_3$ ) is parallel to the direction of  
324 plate motion as indicated in a simple Mohr circle diagram (**A** in Fig. 10a). Before the Chi-Chi  
325 earthquake, the increase of NW-SE directed convergence between the EUP and the PHP (equivalent to  
326 the increase of horizontal principal stress  $\sigma_3$ ) prohibit fault failures. After the Chi-Chi earthquake, the  
327 decrease of NW-SE compression induced normal faulting (**A** in Fig. 9a). The aseismic zone near the  
328 middle part of the Central Range (**B** in Fig. 9b) implies that  $\sigma_1$  is close to vertical, and  $\sigma_2$  is parallel to  
329 the direction of plate convergence (Fig. 10). The intermediate stress,  $\sigma_2$ , increases and decreases before  
330 and after the mainshock, respectively. However, the magnitude of  $\sigma_2$  has no influence on fault failures  
331 (**B** in Fig. 10a). The seismic activity is always low beneath the middle part of the Central Range (Fig.  
332 9). The strike-slip and normal faulting near the southern Central Range (**C** in Fig. 9b) suggest the  
333 magnitude of  $\sigma_1$  is close to  $\sigma_2$  (Fig. 10b). There are more strike-slip events than normal events in  
334 southern Central Range before the Chi-Chi earthquake; while after the Chi-Chi earthquake, we find the  
335 opposite (more normal events than strike slip events) (Fig. 9). This implies that the  $\sigma_1$  become more  
336 aligned with the vertical direction after the Chi-Chi earthquake. Indeed, we find that the ratio of  
337 principal stress difference,  $\phi$ , is close to 1 in southern Central Range before the Chi-Chi mainshock  
338 (Fig. 7). This represents a transitional stress regime of strike-slip faulting to normal faulting that  
339 required only minor stress fluctuations in stress magnitude to change from one stress regime to the

340 other. Regions with elevations lower than  $\sim 1500$  m, for instance, the Western Foothills and the  
341 Longitudinal Valley (**D**, **E** in Fig. 9b), show little effect in topography that  $\sigma_1$  axes are the maximum  
342 horizontal compressive stress. The focal mechanisms include both thrust-faulting and strike-slip  
343 faulting. The faulting style does not vary a lot before and after the Chi-Chi mainshock. The inferred  
344 directions of principal stress axes in Taiwan are summarized in Fig. 10b.

345 The state of the inferred crustal stress field could be used in seismic cycle modeling as a priori  
346 constrains from independent studies. In addition, we provide constraints for the orientation of the  
347 regional stress which is a key parameter in studies of Coulomb stress change (Toda *et al.*, 1998). Our  
348 results also can apply to the estimates of stress magnitude in the crust by examining how regional stress  
349 field react to the stress perturbations from large earthquakes.

350

## 351 **5. Interseismic strain rates near the rupture area of the 1999 Chi-Chi earthquake**

352 One major goal of using the strain rate field in our study is to identify regions with potential  
353 seismic hazards. We are particular interested in seeking for variations of strain-rate and seismicity  
354 before the 1999  $M_w$  7.6 Chi-Chi earthquake. This earthquake nucleated at 8-10 km depth and generated  
355 a 100 km-long surface rupture. Yu *et al.* (2001) analyze preseismic GPS data and conclude that there  
356 are no abnormal signals in GPS position time series before the occurrence of the Chi-Chi earthquake.  
357 Therefore, we focus on investigating the spatial variation of the secular strain-rate and seismicity using  
358 GPS observations and earthquake data before the Chi-Chi mainshock.

359 The region near the Chi-Chi coseismic rupture is characterized with a moderate shortening rate of  
360 25 mm/yr in a 40-km-wide zone from eastern boundary of the Western Foothill to the Coastal Plain  
361 (Fig. 4c). The most distinct feature in this region is that areas with high seismicity (mostly  $M_L < 4$ )  
362 surround the Taichung basin in the interseismic period (Fig. 8). The location of this seismic zone  
363 indicates the boundary of the contraction area to the west and the extension area to the east in central  
364 Taiwan (Fig. 8). This seismic zone is also consistent with the location of western limit of décollement  
365 (Fig. 8) that slips at a rate of about 30 mm/yr over the interseismic period (Dominguez *et al.*, 2003; Hsu  
366 *et al.*, 2003). Because of high stress concentration on the tip of décollement, the level of small  
367 magnitude seismic activity is high. Previous kinematic modeling using interseismic GPS velocity field  
368 suggest that the western end of the décollement is the locked area where major earthquakes might occur  
369 (Dominguez *et al.*, 2003; Hsu *et al.*, 2003), and their results are surprisingly consistent with the rupture  
370 area of the Chi-Chi earthquake (Fig. 8). Our study infers a high contraction rate of about  $0.6 \mu\text{strain/yr}$   
371 in central Taiwan corresponding to the Chi-Chi rupture area as well.

372 It is worth noting that the strain rate in the rupture area of Chi-Chi earthquake is not the largest, in  
373 particular, rates are higher in SW Taiwan and the Longitudinal Valley. The interseismic strain rate may  
374 be greater than the average strain rate of the seismic cycle after the earthquake; while it becomes  
375 smaller than the average before the next future earthquake (Segall, 2002). Obviously, areas with small  
376 strain rate in the interseismic period still have potential to generate large earthquakes, either they are in  
377 a late stage of the seismic cycle or they need longer strain accumulation period.

378 We find most shallow earthquakes locate near the mountain front in western Taiwan; while the  
379 shallow seismicity primary distribute to the east of the Coastal Range in eastern Taiwan (Fig. 8).  
380 According to the historic earthquakes in past century and the characteristics of seismicity distribution in  
381 central Taiwan, small earthquakes tend to surround the locked fault zone in the interseismic period. The  
382 future earthquake probabilities are high in the western Taiwan and the Longitudinal Valley. To have a  
383 better estimate of possible earthquake rupture sources in these regions, we need to carefully investigate  
384 all available geodetic, seismological, as well as geological data.

385

## 386 **6. Conclusion**

387 We use the interseismic GPS velocity field between 1993 and 1999 to estimate the strain-rate field.  
388 Our new approach of strain-rate calculation takes account of the contribution of variable station density  
389 from the distribution of Voronoi cells and avoids dominating results by dense pockets of observations.  
390 The strain-rate field shows that the Longitudinal Valley and SW Taiwan have high NW-SE-directed  
391 contraction in contrast to high NW-SE to NEE-SWW-directed extensions in NE Taiwan and southern  
392 Central Range, respectively. The first-order pattern of the strain-rate field is consistent with previous  
393 studies. In addition, we conduct the stress tensor inversion using earthquake focal mechanisms to  
394 obtain the crustal stress field. The consistency of orientations in principal strain-rate and stress axes  
395 suggests that a large scale variation of stress orientations from the surface to the base of the crust is

396 insignificant. The stress and strain-rate axes in western Taiwan show a fan-shaped pattern. However,  
397 we find that the shape of the Chinese continental margin alone can not fully explain the distribution of  
398 maximum contractive and compressive axes in Taiwan. Extension in the Central Range reflects the  
399 consequence of exhumation and crustal thickening. The seismicity and focal mechanisms before and  
400 after the Chi-Chi earthquake imply that the high topography in the Central Range have changed the  
401 maximum principal stress axis to be vertically orientated. Analyses of geodetic and seismological data  
402 before the 1999 Chi-Chi earthquake shows the consistency between the inferred locked zone and the  
403 Chi-Chi coseismic rupture area. Integrating studies using all available data is important to shed new  
404 light on earthquake rupture sources.

405

#### 406 **Acknowledgments**

407 We are grateful to many colleagues at the Institute of Earth Sciences, Academia Sinica who have  
408 participated in collecting GPS data. The generous provision of continuous GPS data by Ministry of the  
409 Interior, National Cheng-Kung University, National Chiao-Tung University and IGS community are  
410 greatly appreciated. We thank the editor, Dr. D. Brown, Dr. J. Malavieille and an anonymous reviewer  
411 for their constructive comments, Y. M. Wu kindly provide earthquake focal mechanisms, J.-P. Avouac  
412 and W. T. Liang provide valuable suggestions. Several figures were created using GMT written by  
413 Wessel and Smith. This study are supported by the Institute of Earth Sciences, Academia Sinica, the

414 National Science Council of the Republic of China grant NSC 95-2119-M-001-064-MY3 and NSC  
415 95-2745-M-001-005, the National Science Foundation grant EAR-0537625 to Caltech, and the Gordon  
416 and Betty Moore Foundation. This is a contribution of the Institute of Earth Sciences, Academia Sinica,  
417 IESAS1287, Caltech Seismological Laboratory contribution number 10004, and Caltech Tectonics  
418 Observatory number 84.

ACCEPTED MANUSCRIPT

419 **Reference**

- 420 Angelier, J., E. Barrier, and H. T. Chu, 1986. Plate collision and paleostress trajectories in a fold thrust  
421 belt - the foothills of Taiwan, *Tectonophysics*, *125*, 161-178.
- 422 Barrier, E., and J. Angelier, 1986. Active collision in eastern Taiwan - the Coastal Range,  
423 *Tectonophysics*, *125*, 39-72.
- 424 Biq, C. C., 1972. Dual trench structure in the Taiwan-Luzon region, *Proc. Geol. Soc. China*, *15*, 65-75.
- 425 Bollinger, L., J. P. Avouac, R. Cattin, and M. R. Pandey, 2004. Stress buildup in the Himalaya, *J.*  
426 *Geophys. Res.*, *109*, doi:10.1029/2003JB002911.
- 427 Bos, A. G., W. Spakman, and M. C. J. Nyst, 2003. Surface deformation and tectonic setting of Taiwan  
428 inferred from a GPS velocity field, *J. Geophys. Res.*, *108*, doi:10.1029/2002JB002336.
- 429 Chang, C. P., T. Y. Chang, J. Angelier, H. Kao, J. C. Lee, and S. B. Yu, 2003. Strain and stress field in  
430 Taiwan oblique convergent system: constraints from GPS observation and tectonic data, *Earth*  
431 *Planet. Sci. Lett.*, *214*, 115-127.
- 432 Crespi, J. M., Y. C. Chan, and M. S. Swaim, 1996. Synorogenic extension and exhumation of the  
433 Taiwan hinterland, *Geology*, *24*, 247-250.
- 434 Dominguez, S., J. P. Avouac, and R. Michel, 2003. Horizontal coseismic deformation of the 1999  
435 Chi-Chi earthquake measured from SPOT satellite images: Implications for the seismic cycle  
436 along the western foothills of central Taiwan, *J. Geophys. Res.*, *108*, doi:10.1029/2001JB000951.
- 437 Gourley, J. R., 2006. Syn-tectonic extension and lateral extrusion in Taiwan: the tectonic response to  
438 a basement high promontory, University of Connecticut, Ph.D. dissertation, pp.129.
- 439 Gourley, J. R., T. Byrne, Y. C. Chan, F. Wu, and R. J. Rau, 2007. Fault geometries illuminated from  
440 seismicity in central Taiwan: Implications for crustal scale structural boundaries in the northern  
441 Central Range, *Tectonophysics*, *445*, 168-185.
- 442 Ho, C. S., 1986. A synthesis of the geologic evolution of Taiwan, *Tectonophysics*, *125*, 1-16.
- 443 Hsu, T. L., 1976. Neotectonics of the Longitudinal Valley, eastern Taiwan, *Bull. Geol. Surv. Taiwan*, *25*,  
444 53-62.
- 445 Hsu, Y. J., M. Simons, S. B. Yu, L. C. Kuo, and H. Y. Chen, 2003. A two-dimensional dislocation model  
446 for interseismic deformation of the Taiwan mountain belt, *Earth Planet. Sci. Lett.*, *211*, 287-294.
- 447 Hu, J. C., J. Angelier, J. C. Lee, T. H. Chu, and D. Byrne, 1996. Kinematics of convergence,  
448 deformation and stress distribution in the Taiwan collision area: 2-D finite-element numerical  
449 modelling, *Tectonophysics*, *255*, 243-268.
- 450 Hu, J. C., C. S. Hou, L. C. Shen, Y. C. Chan, R. F. Chen, C. Huang, R. J. Rau, K. H. H. Chen, C. W. Lin,  
451 M. H. Huang, and P. F. Nien, 2007. Fault activity and lateral extrusion inferred from velocity field  
452 revealed by GPS measurements in the Pingtung area of southwestern Taiwan, *J Asian Earth Sci*,  
453 *31*, 287-302.
- 454 Huang, C. Y., W. Y. Wu, C. P. Chang, S. Tsao, P. B. Yuan, C. W. Lin, and K. Y. Xia, 1997. Tectonic  
455 evolution of accretionary prism in the arc-continent collision terrane of Taiwan, *Tectonophysics*,

- 456 281, 31-51.
- 457 Hugentobler, U., S. Schaer, and P. Fridez 2001. Bernese GPS software v. 4.2, Astronomical Institute,  
458 University of Berne, Switzerland, 515pp.
- 459 Kao, H., and P. R. Jian, 2001. Seismogenic patterns in the Taiwan region: insights from source  
460 parameter inversion of BATS data, *Tectonophysics*, 333, 179-198.
- 461 Kim, K. H., J. M. Chiu, J. Pujol, K. C. Chen, B. S. Huang, Y. H. Yeh, and P. Shen, 2005.  
462 Three-dimensional V-P and V-S structural models associated with the active subduction and  
463 collision tectonics in the Taiwan region, *Geophys. J. Int.*, 162, 204-220.
- 464 Lacombe, O., F. Mouthereau, J. Angelier, and B. Deffontaines, 2001. Structural, geodetic and  
465 seismological evidence for tectonic escape in SW Taiwan, *Tectonophysics*, 333, 323-345.
- 466 Lin, A. T., and A. B. Watts, 2002. Origin of the West Taiwan basin by orogenic loading and flexure of a  
467 rifted continental margin, *J. Geophys. Res.*, 107.
- 468 Lin, C. H., 2000. Thermal modeling of continental subduction and exhumation constrained by heat  
469 flow and seismicity in Taiwan, *Tectonophysics*, 324, 189-201.
- 470 Liu, T. K., 1982. Tectonic implication of fission track ages from the Central Range, Taiwan, *Proc. Geol.*  
471 *Soc. China*, 25, 22-37.
- 472 Lu, C. Y., and J. Malavieille, 1994. Oblique convergence, indentation and rotation tectonics in the  
473 Taiwan mountain belt - insights from experimental modeling, *Earth Planet. Sci. Lett.*, 121,  
474 477-494.
- 475 Matthews, M. V., and P. Segall, 1993. Estimation of depth-dependent fault slip from measured surface  
476 deformation with application to the 1906 San-Francisco earthquake, *J. Geophys. Res.*, 98,  
477 12153-12163.
- 478 Meng, G. Y., 1971. A conception of the evolution of the island of Taiwan and its bearing on the  
479 development of the western Neogene sedimentary basin, *Petrol. Geol. Taiwan*, 9, 241-258.
- 480 Michael, A. J., 1984. Determination of stress from slip data - faults and folds, *J. Geophys. Res.*, 89,  
481 1517-1526.
- 482 Michael, A. J., 1987. Use of focal mechanisms to determine Stress - a control study, *J. Geophys. Res.*,  
483 92, 357-368.
- 484 Segall, P., 2002. Integrating geologic and geodetic estimates of slip rate on the San Andreas fault  
485 system, *Int. Geology Rev.*, 44, 62-82.
- 486 Seno, T., S. Stein, and A. E. Gripp, 1993. A model for the Motion of the Philippine Sea Plate consistent  
487 with Nuvel-1 and geological Data, *J. Geophys. Res.*, 98, 17941-17948.
- 488 Shen, Z. K., D. D. Jackson, and B. X. Ge, 1996. Crustal deformation across and beyond the Los  
489 Angeles basin from geodetic measurements, *J. Geophys. Res.*, 101, 27957-27980.
- 490 Sibuet, J. C., J. Letouzey, F. Barbier, J. Charvet, J. P. Foucher, T. W. C. Hilde, M. Kimura, L. Y. Chiao,  
491 B. Marsset, C. Muller, and J. F. Stephan, 1987. Back arc extension in the Okinawa trough, *J.*  
492 *Geophys. Res.*, 92, 14041-14063.

- 493 Simoes, M., J. P. Avouac, O. Beyssac, B. Goffe, K. A. Farley, and Y. G. Chen, 2007. Mountain building  
494 in Taiwan: A thermokinematic model, *J. Geophys. Res.*, *112*, doi:10.1029/2006JB004824.
- 495 Stein, S., S. Cloetingh, N. H. Sleep, and R. Wortel, 1989. Passive margin earthquakes, stresses and  
496 rheology. In Earthquakes at North-Atlantic passive margins: neotectonics and postglacial respond,  
497 *NATO ASI Ser. C*, Kluwer Academic, Boston, Mass., pp.231-259.
- 498 Suppe, J., 1984. Kinematics of arc-continent collision, flipping of subduction, and back-arc spreading  
499 near Taiwan, *Mem. Geol. Soc. China*, 21-33.
- 500 Suppe, J., C. T. Hu, and Y. J. Chen, 1985. Present-day stress directions in western Taiwan inferred from  
501 borehole elongation, *Petrol. Geol. Taiwan*, *21*, 1-12.
- 502 Teng, L. S., 1996. Extensional collapse of the northern Taiwan mountain belt, *Geology*, *24*, 949-952.
- 503 Toda, S., R. S. Stein, P. A. Reasenber, J. H. Dieterich, and A. Yoshida, 1998. Stress transferred by the  
504 1995 M-w = 6.9 Kobe, Japan, shock: Effect on aftershocks and future earthquake probabilities, *J.*  
505 *Geophys. Res.*, *103*, 24543-24565.
- 506 Ward, S., 1998. On the consistency of earthquake moment rates, geological fault data, and space  
507 geodetic strain: the United States, *Geophys. J. Int.*, *134*, 172-186.
- 508 Wu, F. T., 1978. Recent tectonics in Taiwan, *J. Phys. Earth*, *26*, 265-299.
- 509 Wu, Y. M., C. H. Chang, L. Zhao, J. B. H. Shyu, Y. G. Chen, K. Sieh, and J. P. Avouac, 2007. Seismic  
510 tomography of Taiwan: Improved constraints from a dense network of strong motion stations, *J.*  
511 *Geophys. Res.*, *112*, doi:10.1029/2007JB004983.
- 512 Wu, Y. M., L. Zhao, C. H. Chang, and Y. J. Hsu, 2008. Focal-mechanism determination in Taiwan by  
513 genetic algorithm, *Bull. Seismol. Soc. Am.*, *98*, 651-661.
- 514 Yeh, Y. H., E. Barrier, C. H. Lin, and J. Angelier, 1991. Stress tensor analysis in the Taiwan area from  
515 focal mechanisms of earthquakes, *Tectonophysics*, *200*, 267-280.
- 516 Yu, S. B., and H. Y. Chen, 1994. Global Positioning System measurements of crustal deformation in the  
517 Taiwan arc-continent collision zone, *TAO*, *5*, 477-498.
- 518 Yu, S. B., H. Y. Chen, and L. C. Kuo, 1997. Velocity field of GPS stations in the Taiwan area,  
519 *Tectonophysics*, *274*, 41-59.
- 520 Yu, S. B., and L. C. Kuo, 2001. Present-day crustal motion along the Longitudinal Valley Fault, eastern  
521 Taiwan, *Tectonophysics*, *333*, 199-217.
- 522 Zoback, M. L., 1992. First- and second-order patterns of stress in the lithosphere: The world stress map  
523 project *J. Geophys. Res.*, *97*, 11703-11728.

524  
525  
526  
527  
528  
529

530 **Figure captions**

531 Figure 1 Tectonic setting in the Taiwan plate boundary zone. In the north, the Philippine Sea plate  
532 subducts beneath the Ryukyu Arc; while to the south, the South China Sea block of the Eurasian  
533 plate subducts beneath the Philippine Sea plate. The grey colors show the shaded relief topography  
534 and bathymetry. Hatched area indicates the Peikang basement high in the Chinese continental  
535 margin.

536

537 Figure 2 Taiwan GPS velocity field relative to Paisha, Penghu between 1993 and 1999. Blue and red  
538 vectors with 95% confidence ellipses show velocities of sites located to the west and to the east of  
539 the Longitudinal fault (LVF), respectively. The grey color shaded relief indicates the topography.  
540 Major faults are indicated as black lines. White dots correspond to GPS stations. The star denotes the  
541 epicenter of 1999 Chi-Chi earthquake. The area between the CLPF and the yellow line indicates the  
542 region where the Chi-Chi coseismic slip is larger than 1 m

543

544 Figure 3 The Voronoi diagram associated with the distribution of GPS sites used in this study. (a)  
545 The Voronoi cell (polygon) associated with each site indicates the region represented by that  
546 particular site. (b) The Voronoi diagram modified to remove extension of the cells off shore.

547

548 Figure 4 (a) Observed and interpolated GPS velocities shown as black and red vectors, respectively; (b)  
549 Residual velocities after removal of the interpolated field; (c) Dilatation and principal strain rates.  
550 The color scale indicates dilatation rate in  $\mu\text{strain/yr}$ . Black (contraction) and grey (extension)  
551 vectors denote the two principal strain-rate axes. Major faults are indicated as green lines. The star  
552 denotes the epicenter of 1999 Chi-Chi earthquake. (d) One standard deviation in  $\mu\text{strain/yr}$  for the  
553 dilatation rate. The base of foreland basin is indicated in red contours at intervals of 1 km. The  
554 azimuths of maximum contractional strain-rate axes are shown in grey contours at intervals of  $20^\circ$ .

555 Note that the azimuth counts from the north, counterclockwise rotation is negative.

556

557 Figure 5 Results of the stress tensor inversions. Squares, triangles, and circles represent three principal  
 558 stress axes,  $\sigma_1$ ,  $\sigma_2$  and  $\sigma_3$ , in equal-area projection of the lower hemisphere. The best solution is  
 559 marked by large symbols with white outlines. The small symbols show the distribution of stress  
 560 axes within 95% confidence region.

561

562 Figure 6 The principal strain-rate (black) and stress (red) axes. Surface projections of the  $\sigma_1$  and  $\sigma_3$  axes  
 563 are the largest when the plunges are  $0^\circ$  (horizontal) and are close to 0 when the plunges are  $90^\circ$   
 564 (vertical).

565

566 Figure 7 Grey color and texts denote the ratio of principal stress difference  $\phi = \frac{\sigma_2 - \sigma_3}{\sigma_1 - \sigma_3}$  from the  
 567 stress tensor inversion. If  $\sigma_1 = \sigma_2$ , namely  $\phi = 1$ , corresponds to a stress regime transitional to  
 568 normal faulting; while if  $\sigma_2 = \sigma_3$ , namely  $\phi = 0$ , corresponds to a stress regime transitional to thrust  
 569 faulting.

570

571 Figure 8 The seismicity and dilatation rate in the Taiwan area. The seismicity with  $M_L > 3$  between 1990  
 572 and 1999.7 is located by the Central Weather Bureau (CWB) seismic network in Taiwan. Color  
 573 circle indicates earthquake focal depth and its size is proportional to the magnitude.. The red and  
 574 blue colors show the dilatation field in Figure 4c. The area between the CLPF and the light blue  
 575 line indicates the region where the Chi-Chi coseismic slip is larger than 1 m. The purple dash line  
 576 shows the western end of interseismic slip on the décollement from Hsu et al. (2003).

577

578 Figure 9 Earthquake focal mechanisms with  $M_L > 4$  and Depth < 30 km from Wu et al. (2008) (a) Focal

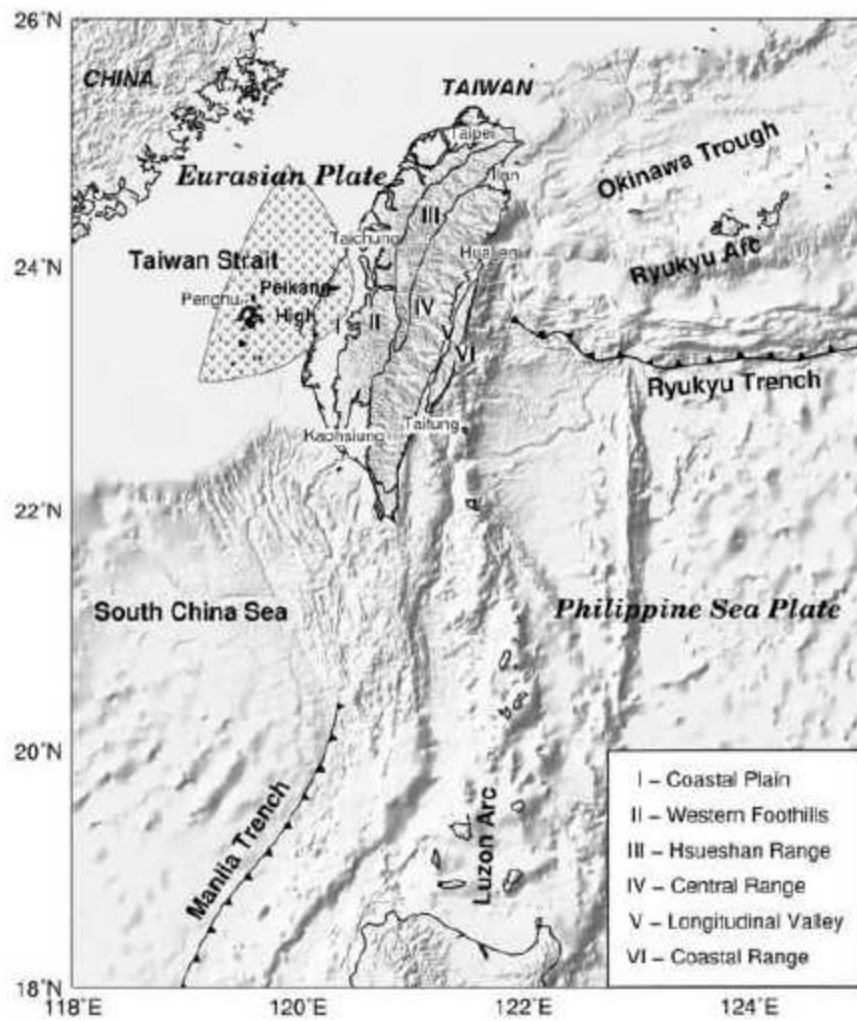
579 mechanisms before and after 1999.7 (the Chi-Chi earthquake) are shown as blue and red,  
580 respectively; The green and blue lines denote the CLPF and the elevation of 1500 m, respectively;  
581 (b) Focal mechanisms between 1999.7 and 2001.7 (after the Chi-Chi earthquake).

582

583 Figure 10 The orientations of principal stress axes (a) The Mohr circle represents the stress of the crust  
584 in area *A* and *B* denoted in Figure 9b. The straight line indicates the strength of the crust; (b)  
585 Inferred stress axes from seismicity distribution and focal mechanisms

ACCEPTED MANUSCRIPT

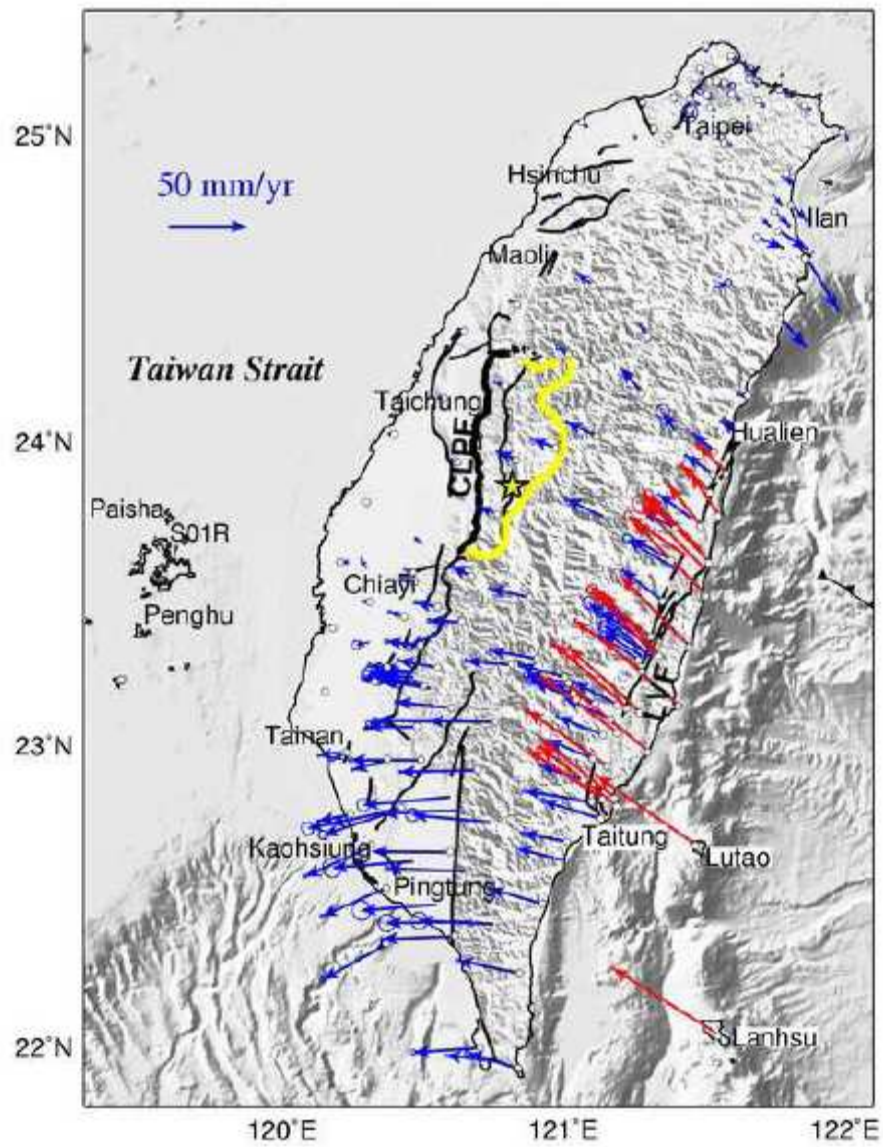
586 Fig 1



587

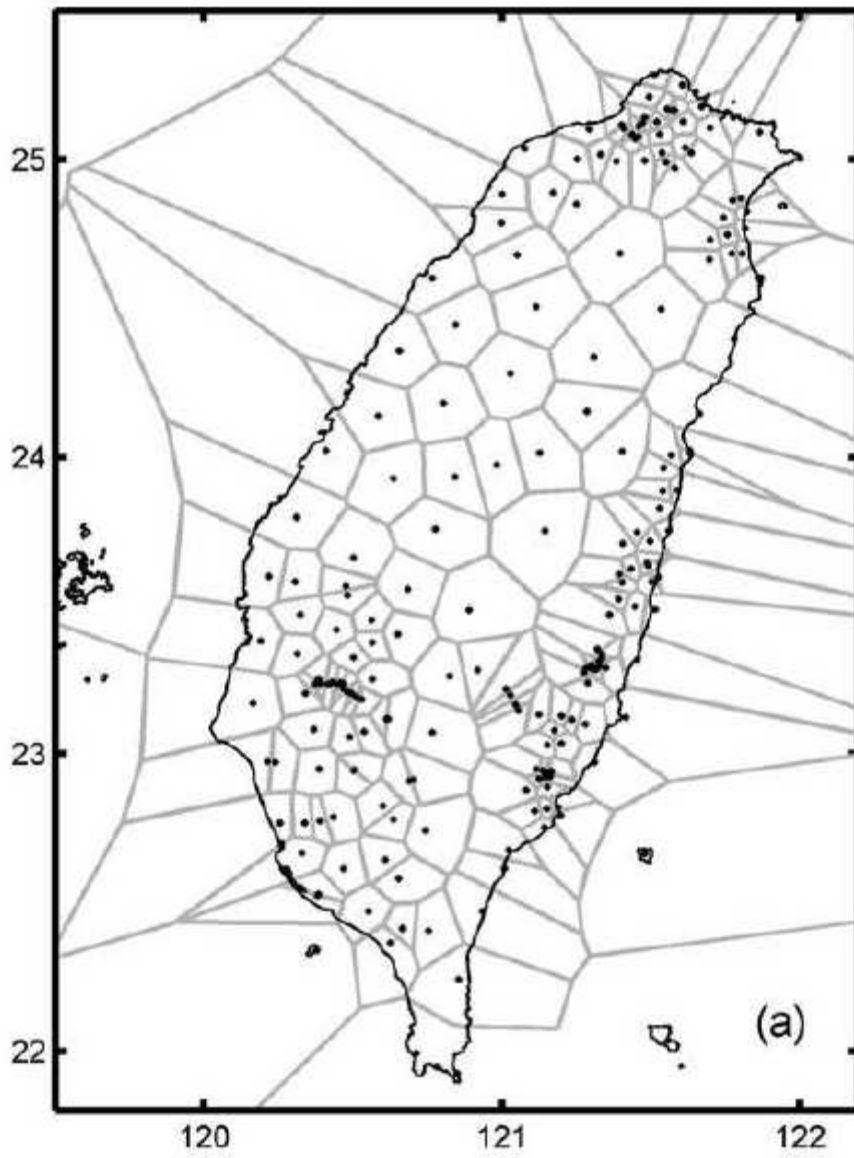
A

588 Fig 2



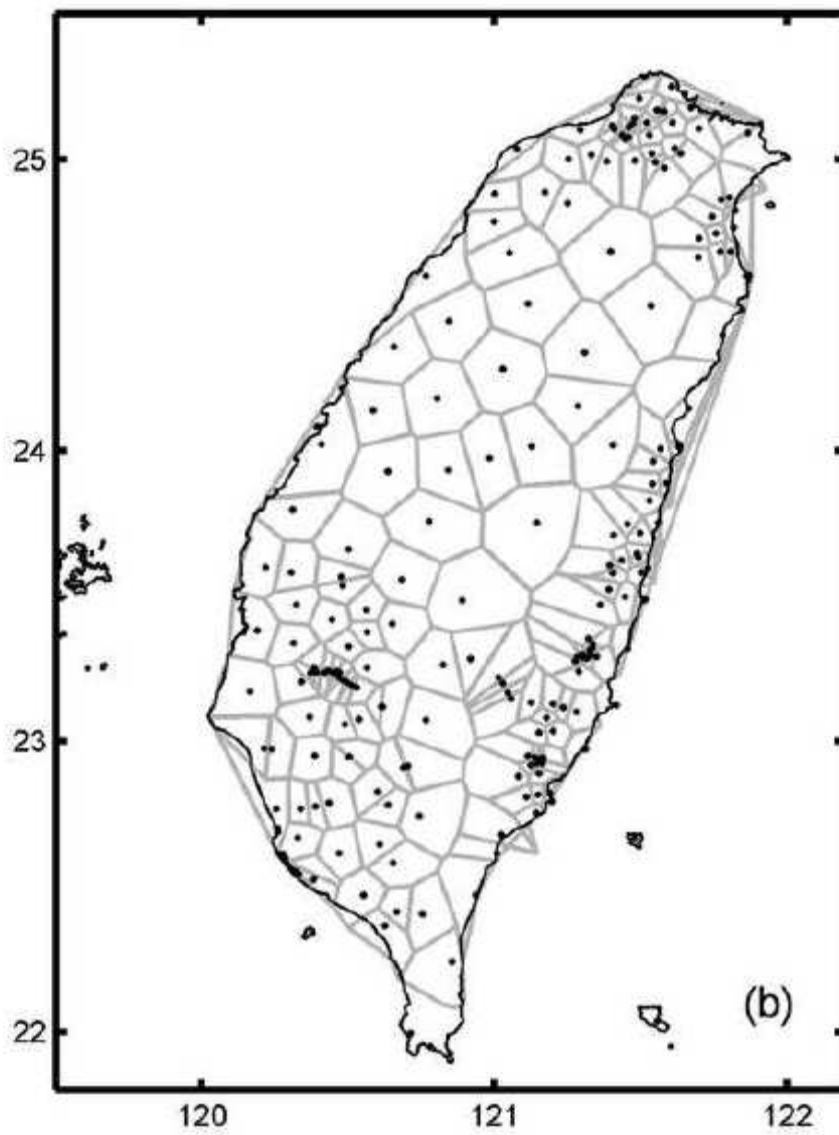
589

590 Fig 3a



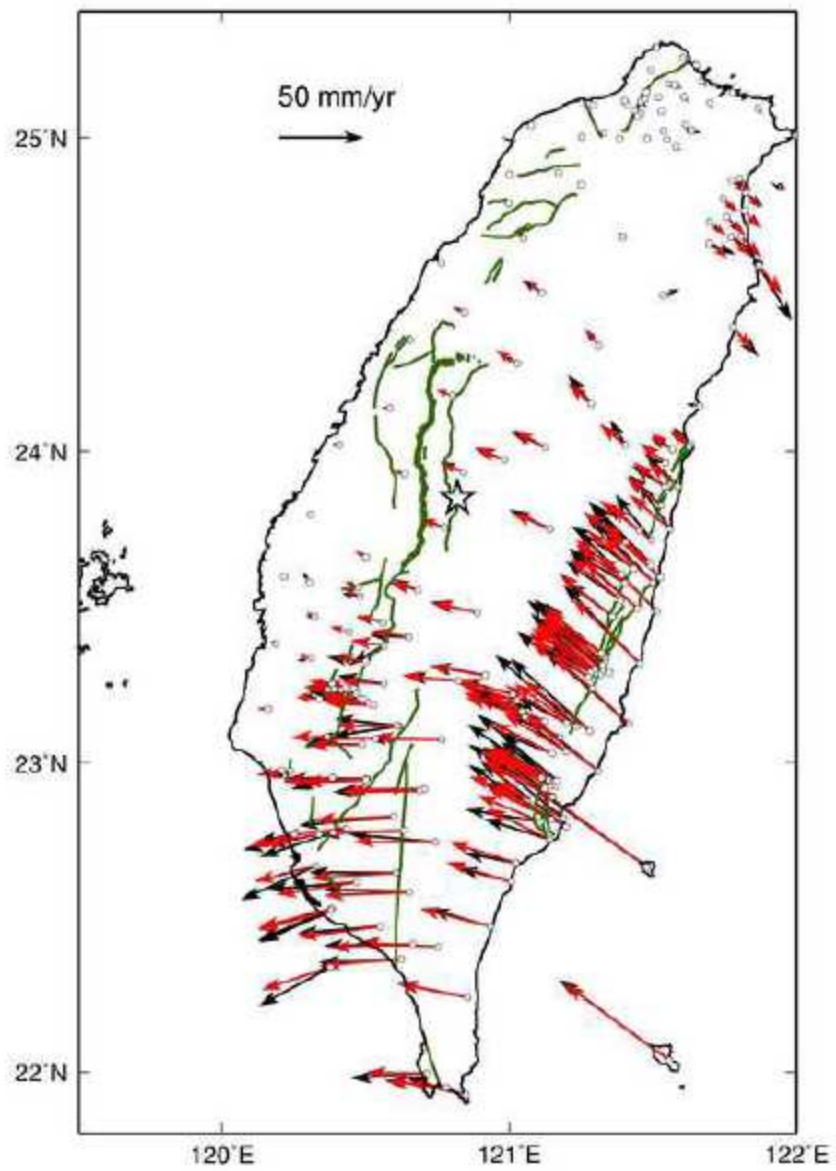
591

592 Fig 3b



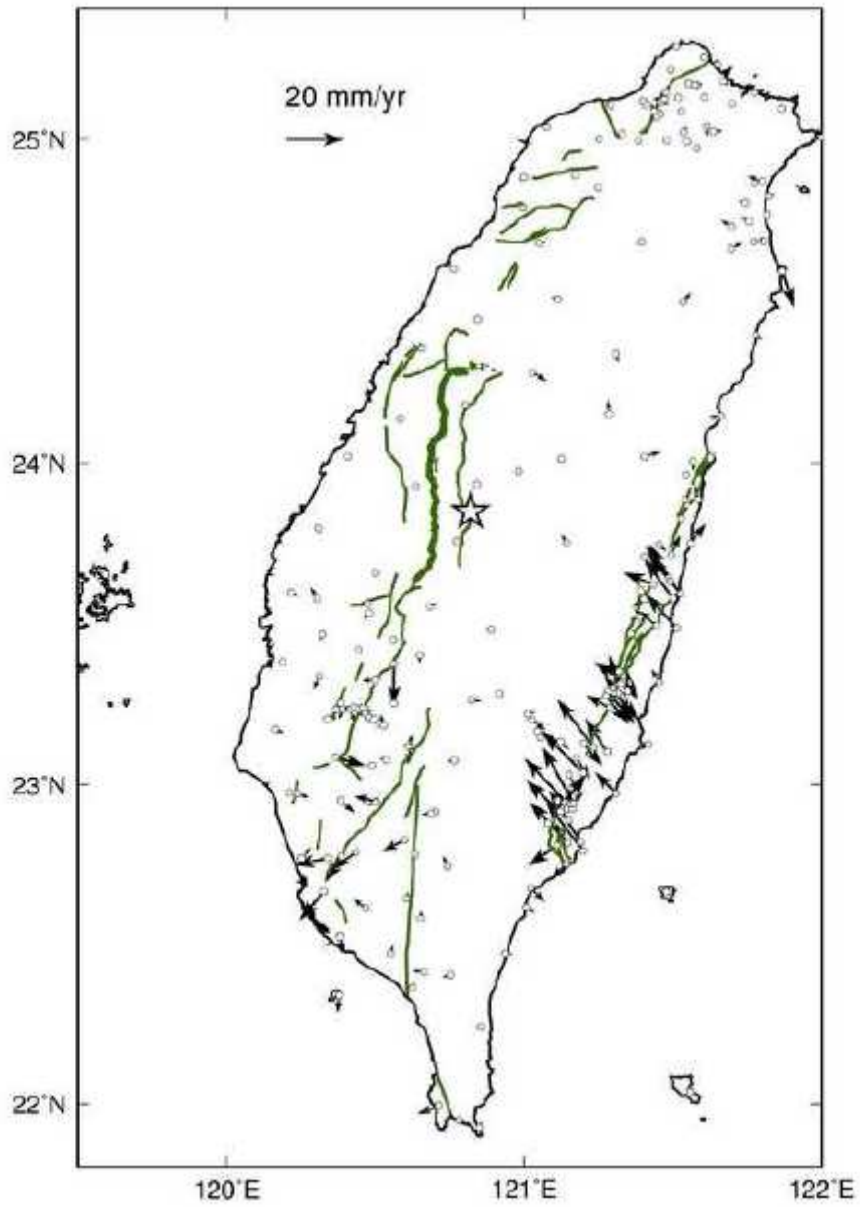
593

594 Fig 4a



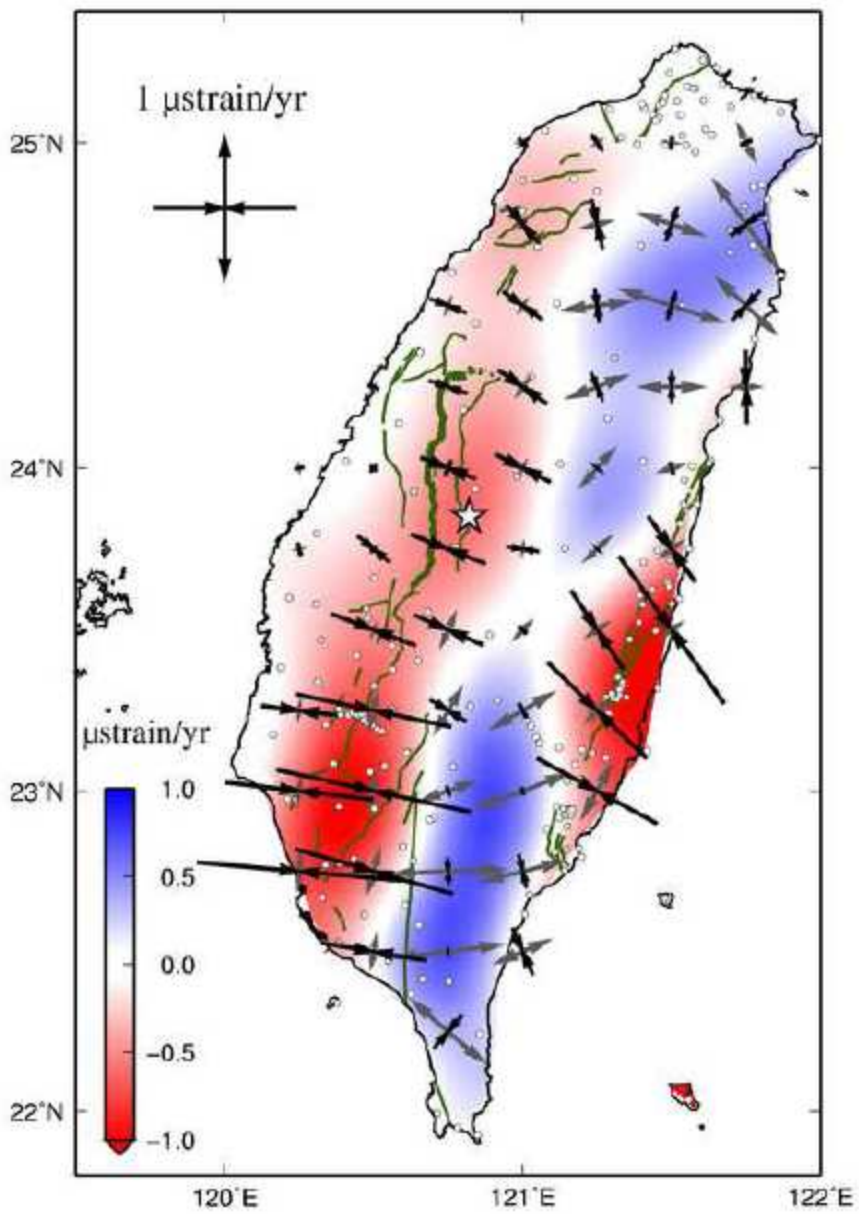
595

596 Fig 4b



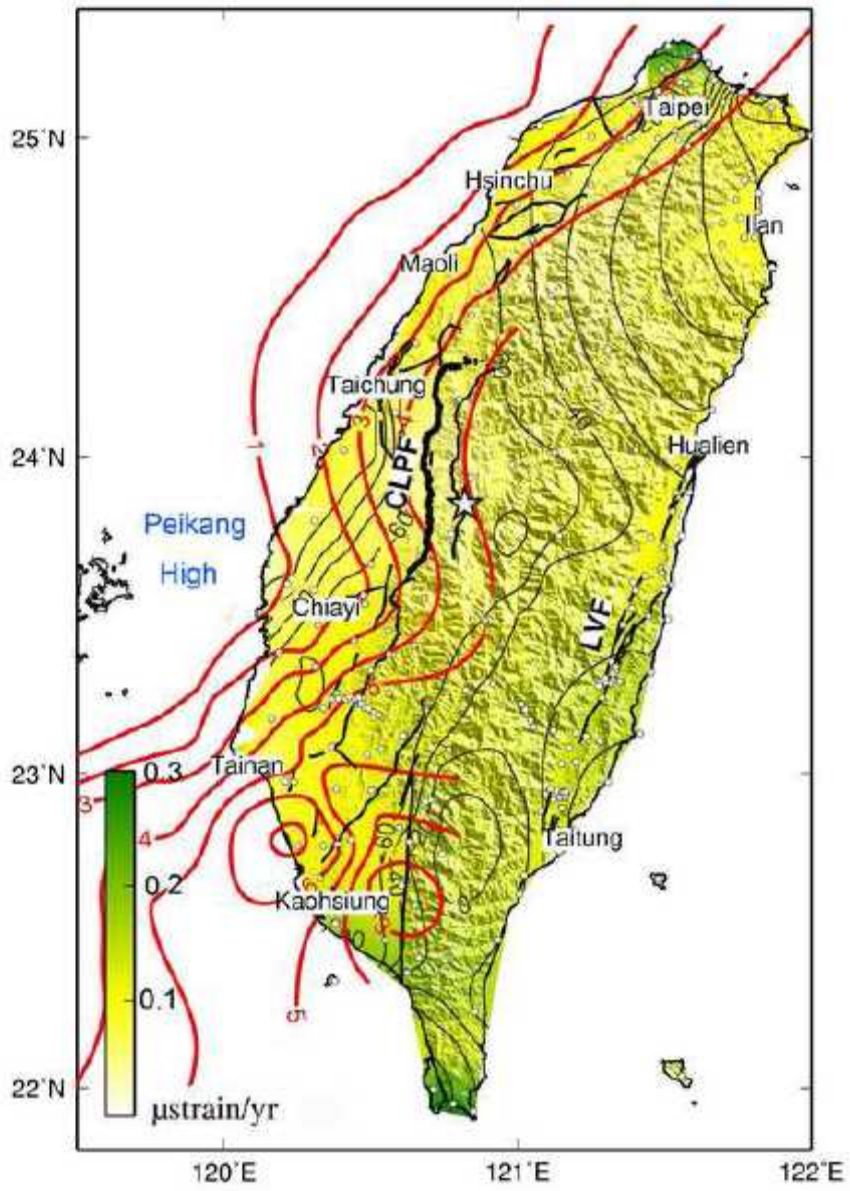
597

598 Fig 4c



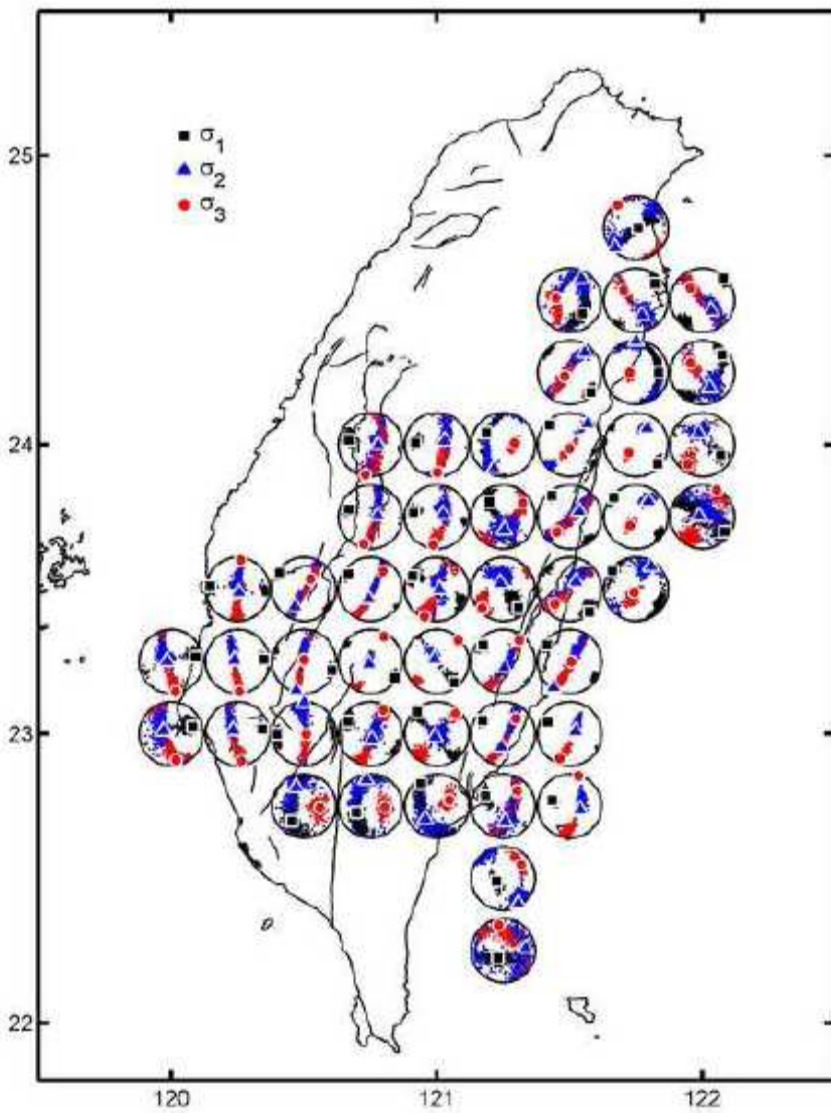
599

600 Fig 4d



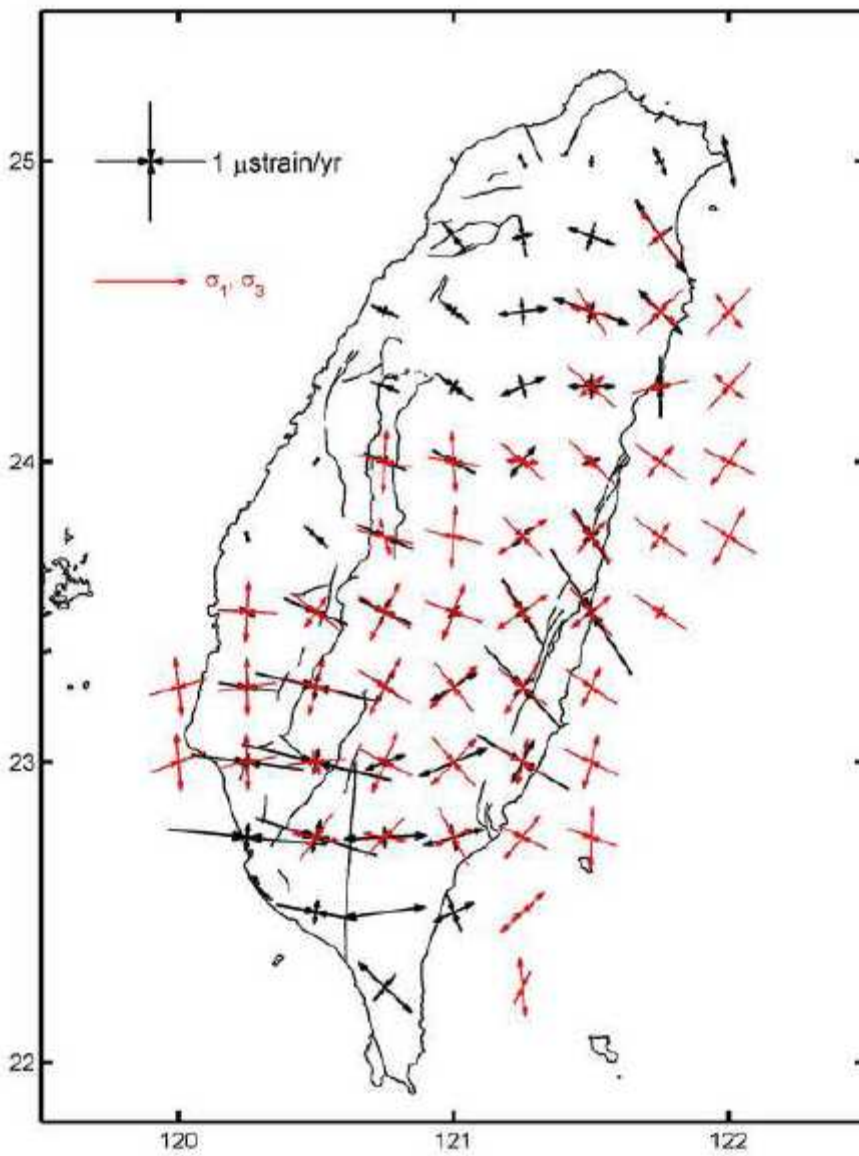
601

602 Fig 5



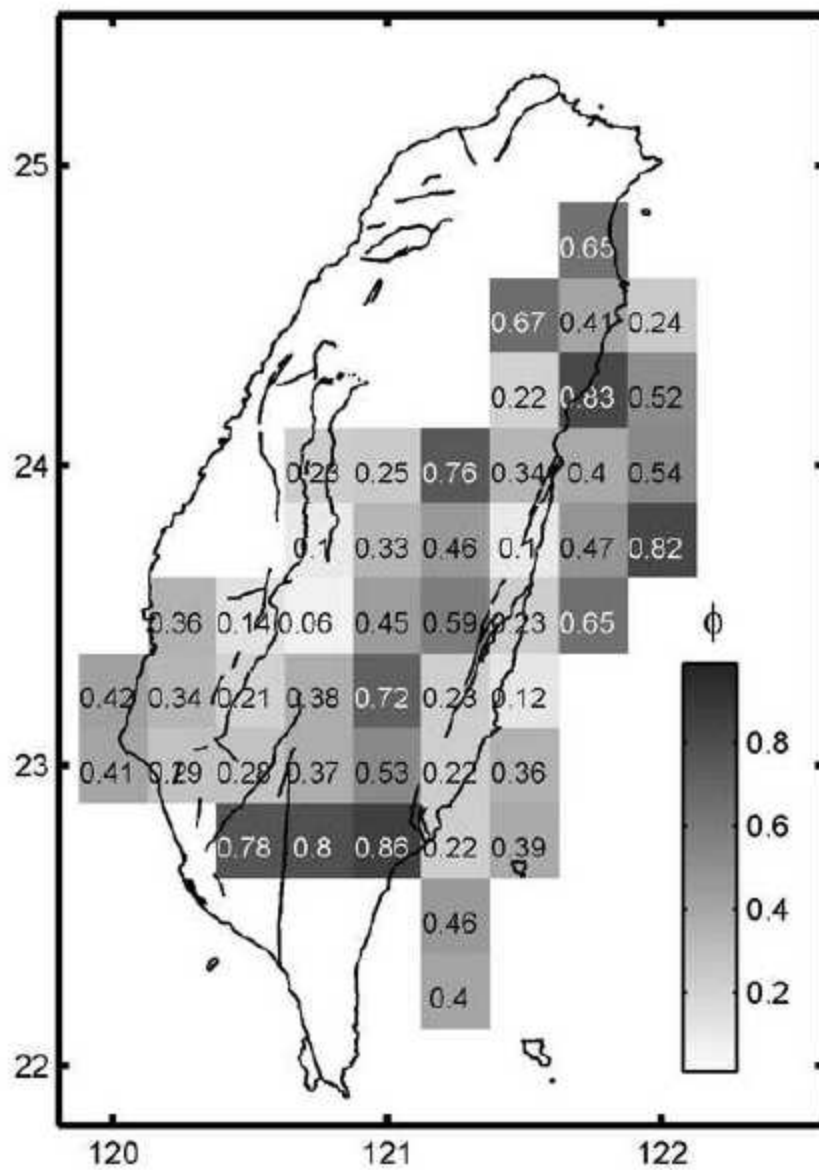
603

604 Fig 6



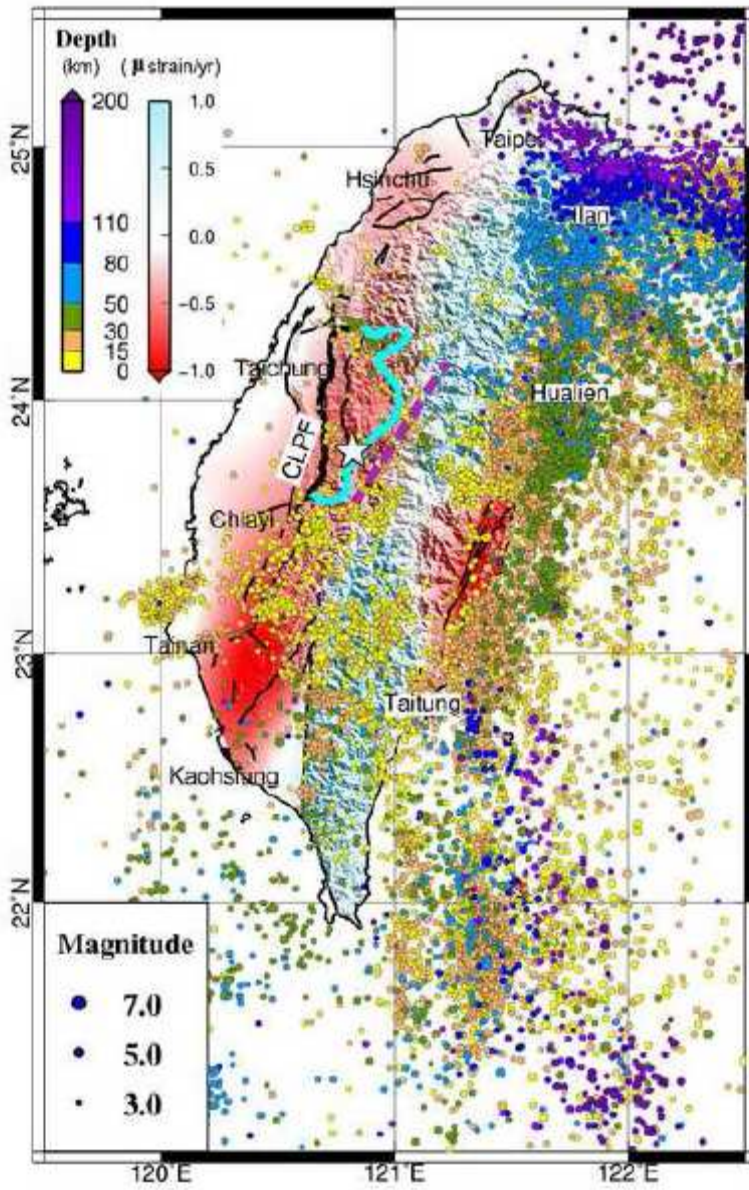
605

606 Fig 7



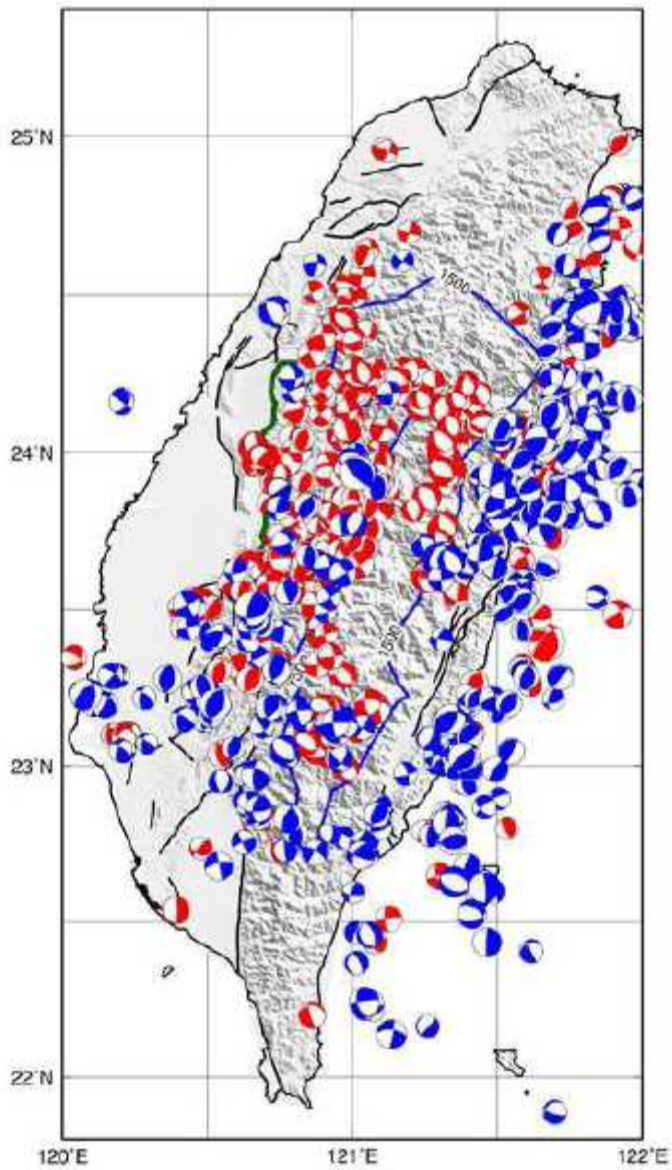
607

608 Fig 8



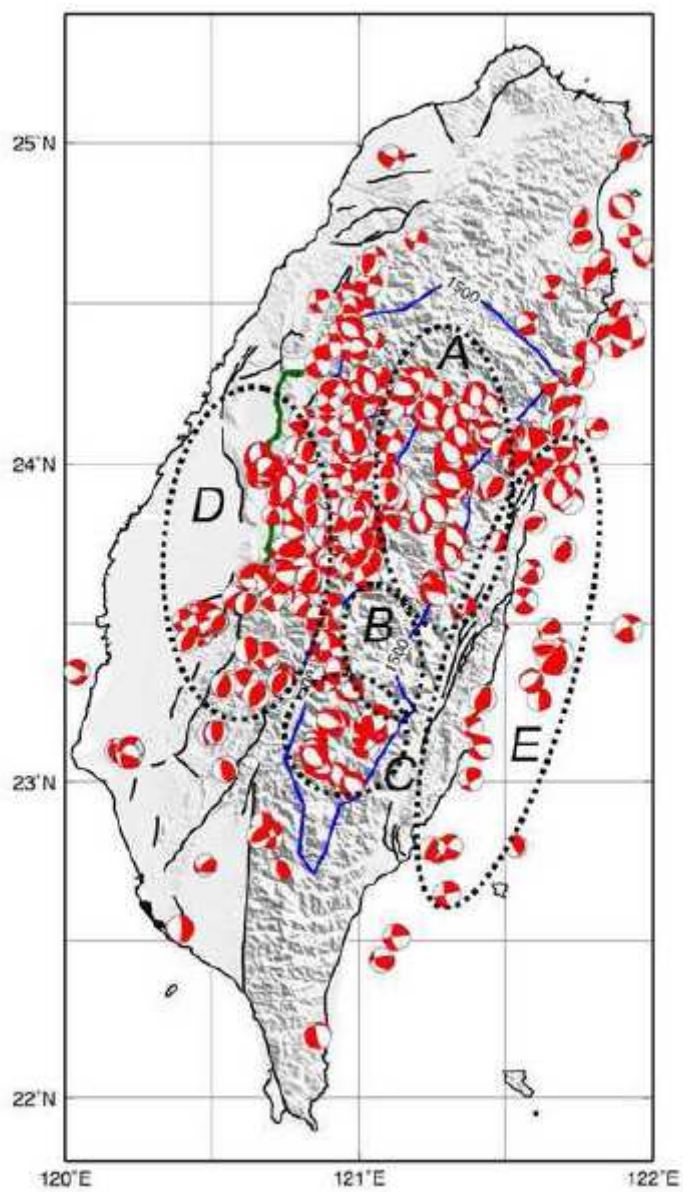
609

610 Fig 9a



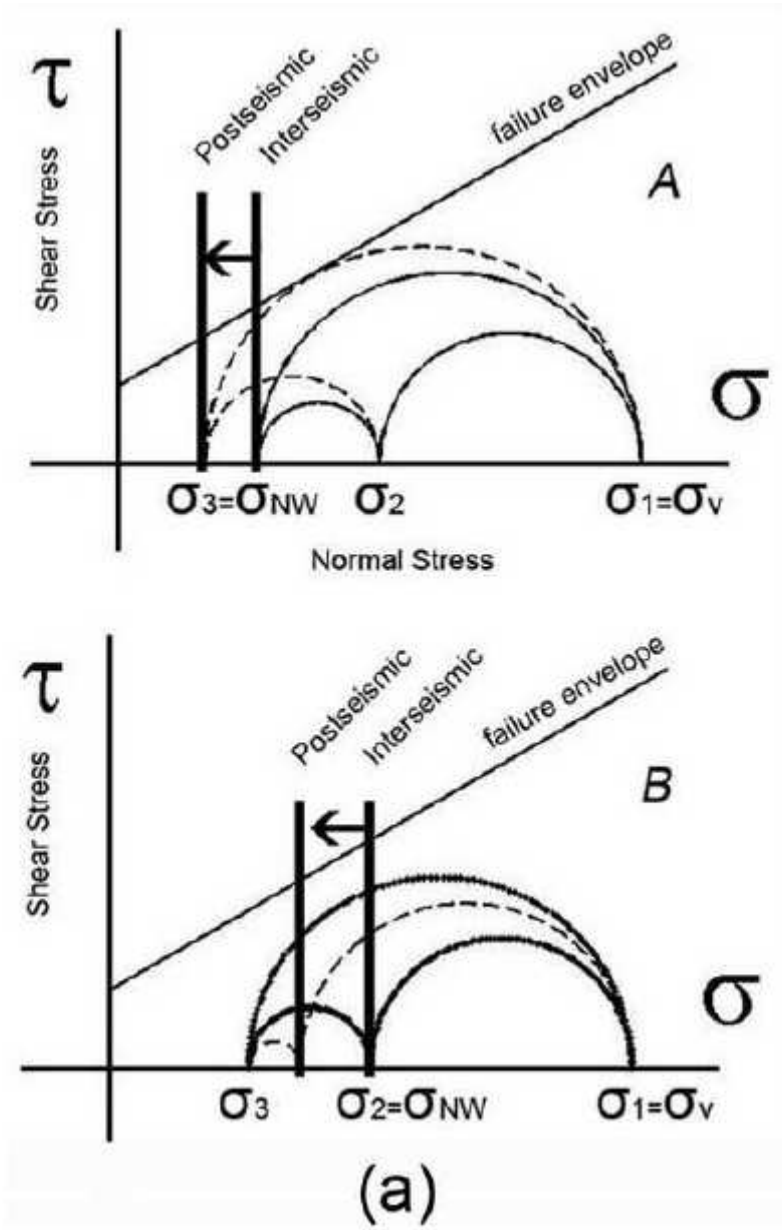
611

612 Fig 9b



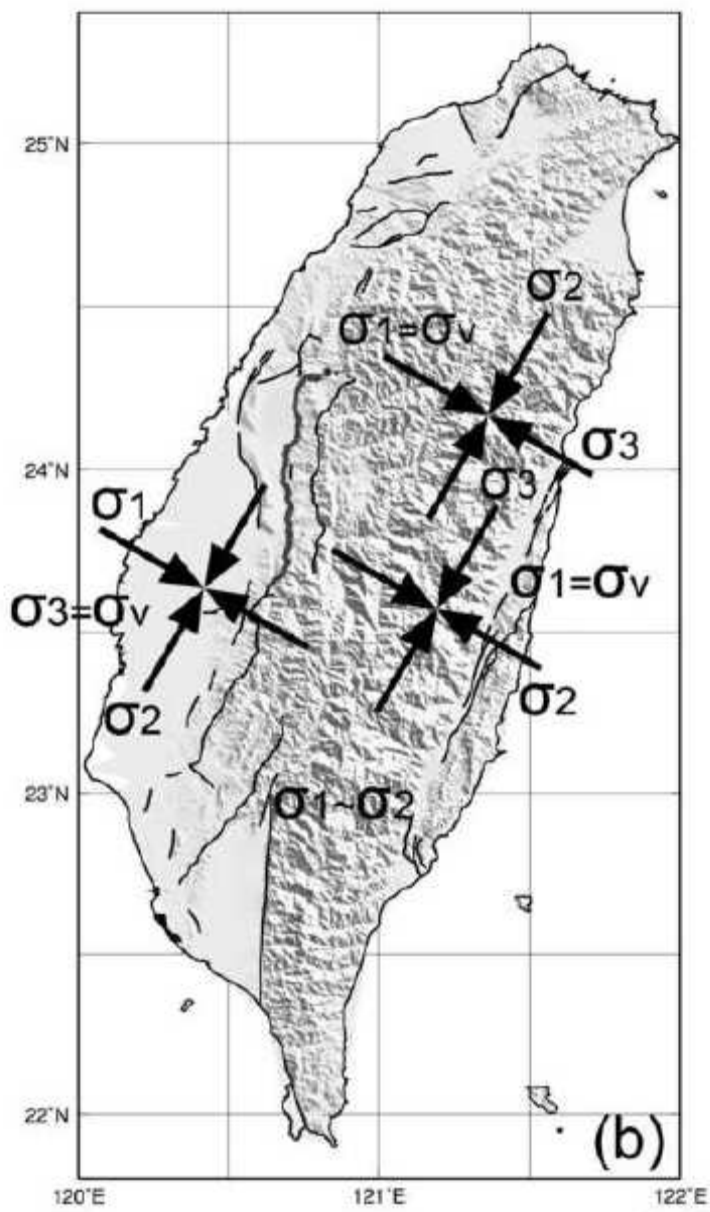
613

614 Fig 10a



615

616 Fig 10b



617

618 Table 1. Station velocity with respect to Paisha, Penghu (S01R) on two sides of the Longitudinal

619 Valley fault (LVF)

620

Station	Longitude (°)	Latitude (°)	$V$ (mm/yr)	$Azi$ (°)	$a$ (mm/yr)	$b$ (mm/yr)	$Azi_a$ (°)	$n$	time span
<i>Sites to the west of the LVF</i>									
0054	121.1989	23.1286	32.8	298	0.5	0.4	86	8	1993.4-1999.4
0107	120.8442	24.4444	6.3	291	0.3	0.3	85	7	1993.5-1999.6
0131	121.5431	23.9636	19.0	308	0.3	0.3	85	11	1993.4-1999.6
0135	121.3486	23.2908	55.8	317	0.5	0.4	78	8	1993.4-1999.4
0201	121.3200	23.3539	32.8	302	0.9	0.9	67	7	1994.2-1999.4
0206	121.1092	22.8100	45.1	279	0.5	0.5	86	7	1993.4-1999.4
0207	121.1475	22.8178	58.6	303	0.6	0.6	70	6	1993.4-1998.3
0211	121.1419	22.7533	40.9	287	0.5	0.4	91	9	1993.4-1999.4
0216	121.6308	24.0228	14.3	313	0.4	0.3	79	10	1993.4-1999.4
0241	121.3347	23.3361	52.0	310	0.9	0.9	45	6	1994.2-1999.4
0242	121.3250	23.2961	58.3	317	1.4	1.3	45	5	1995.2-1999.4
0283	121.2336	23.1178	64.1	311	0.6	0.6	75	6	1993.4-1998.3
0437	120.4675	23.2369	21.2	275	0.9	0.8	92	6	1993.4-1998.5
0504	121.6975	24.7311	8.3	131	0.3	0.3	86	6	1993.5-1999.6
0505	121.7569	24.7464	11.7	136	0.4	0.4	99	7	1994.9-1999.6
0544	120.6333	22.7828	50.2	268	0.6	0.5	103	7	1995.3-1999.4
0575	120.6639	22.4139	52.7	269	2.3	2.1	94	3	1997.1-1999.4
0621	120.4339	22.7897	48.7	258	0.4	0.3	95	11	1993.4-1999.0
0727	121.3925	23.6056	30.3	298	0.4	0.4	80	9	1993.4-1999.4
0801	121.4936	25.2122	2.2	180	0.4	0.4	116	7	1993.2-1998.9
0971	121.6958	24.6633	16.7	113	0.4	0.3	85	8	1994.9-1999.6
0980	121.1714	24.8889	1.0	249	0.4	0.3	77	9	1993.5-1999.6
0982	121.4575	25.1133	4.8	129	0.4	0.4	91	6	1993.2-1998.9
0991	121.3306	25.0167	1.3	233	0.5	0.5	74	9	1993.2-1998.9
0996	121.8017	24.8706	5.7	167	0.3	0.3	82	10	1993.5-1999.6
1043	121.5486	24.9925	2.2	87	1.1	1.0	109	5	1993.2-1997.9
1045	121.6075	25.1292	4.4	137	0.4	0.4	88	7	1993.2-1998.9
1055	121.6992	25.1089	3.7	147	0.5	0.5	83	6	1993.2-1998.9
1063	121.6700	25.1775	4.4	139	0.4	0.4	79	6	1993.2-1998.9

1064	121.5292	25.0842	1.9	127	0.4	0.3	83	7	1993.2-1998.9
1102	121.4778	25.1442	1.5	132	0.8	0.7	144	4	1995.3-1998.9
1119	121.6039	25.2528	2.6	143	0.5	0.5	39	6	1993.2-1998.9
1139	121.7442	24.8050	9.1	140	0.4	0.4	90	7	1993.5-1999.6
1168	121.7756	25.1431	5.2	124	0.5	0.4	76	9	1993.2-1998.9
1172	121.3156	23.2858	54.2	311	1.7	1.5	1	4	1995.2-1999.4
1178	121.2825	23.2911	29.6	302	1.6	1.6	132	4	1995.2-1999.4
1215	121.5869	23.8878	28.0	316	0.4	0.4	70	8	1993.4-1999.4
13R3	121.3247	23.3144	41.8	306	1.7	1.5	37	5	1995.2-1999.4
13R4	121.2989	23.3017	33.0	302	1.5	1.4	34	4	1995.2-1999.4
1449	121.4044	24.0203	17.4	328	1.9	1.8	96	6	1994.2-1999.6
5936	121.1267	24.0131	22.7	295	0.3	0.2	81	10	1993.5-1999.6
6267	121.3953	24.6844	2.9	330	0.3	0.3	83	7	1994.9-1999.6
6389	121.2847	24.1525	22.2	321	0.3	0.2	85	9	1993.5-1999.6
6636	120.6519	22.5822	50.6	272	0.6	0.6	112	5	1995.3-1999.4
7205	120.7656	23.0750	44.4	271	0.4	0.3	90	14	1993.4-1999.4
8046	121.1764	23.0825	33.8	294	0.6	0.5	88	7	1993.4-1999.4
8152	121.4872	23.6453	48.3	316	1.5	1.2	82	5	1996.1-1999.4
A247	120.4078	24.0206	4.2	276	0.3	0.3	76	7	1993.5-1999.6
C006	120.5367	23.0775	37.3	271	0.7	0.6	114	3	1996.1-1999.0
CHNL	120.5633	23.3772	22.8	241	0.9	0.9	112	8	1997.9-1999.0
CHSN	121.5533	25.1708	2.4	140	0.4	0.4	108	7	1993.2-1998.9
CK01	120.2106	22.9758	14.5	260	0.2	0.2	73	16	1994.1-1999.6
CKLS	121.8656	25.0931	3.0	138	0.4	0.3	73	10	1993.5-1999.6
CPUL	120.6347	23.9275	6.0	287	0.3	0.3	75	10	1993.5-1999.6
FCWS	121.2497	24.8506	2.0	288	0.2	0.1	80	21	1993.5-1999.6
FLNM	121.4533	23.7464	25.8	307	0.2	0.1	92	24	1994.1-1999.6
FONS	120.3817	22.5300	47.4	246	0.5	0.4	87	11	1993.4-1999.4
G013	120.5511	22.4714	48.7	265	2.6	2.4	95	3	1997.1-1999.4
G017	120.5983	22.8272	56.1	265	1.7	1.7	101	4	1997.1-1999.0
G023	120.4686	22.6147	52.7	266	2.6	2.4	95	4	1997.1-1999.4
HTZS	120.9819	23.9739	18.2	291	0.3	0.2	81	9	1993.5-1999.6
I001	121.4789	24.9967	2.1	158	0.4	0.4	78	6	1993.2-1998.9
I004	120.2392	22.9736	11.7	249	0.6	0.5	89	10	1993.4-1998.0
I007	120.7744	23.7561	14.4	292	0.3	0.2	76	15	1993.4-1999.6
I029	121.8167	24.7678	13.0	138	0.3	0.3	81	7	1993.5-1999.6
I042	120.2528	22.7700	22.6	259	0.3	0.3	108	11	1993.4-1999.6

I045	120.3275	22.6675	48.7	246	0.4	0.4	105	11	1993.4-1999.4
I301	121.7717	24.6839	20.7	123	0.4	0.4	100	6	1994.9-1999.6
JFES	120.8417	23.9344	15.1	294	0.4	0.3	76	8	1993.5-1999.6
KDNM	120.7819	21.9494	36.3	277	0.2	0.2	100	22	1994.1-1999.6
KLUN	121.3842	24.9958	0.9	247	0.3	0.3	70	14	1993.2-1999.6
KUYN	121.0761	25.0375	2.5	154	0.4	0.4	89	7	1993.5-1999.6
LIUC	120.3786	22.3408	48.3	241	0.6	0.5	77	8	1993.4-1999.4
MERK	120.3094	23.7975	1.6	215	0.3	0.3	79	14	1993.4-1999.6
N091	121.2522	25.0014	2.5	169	0.5	0.4	102	6	1995.3-1999.6
NCTU	120.9972	24.7889	4.5	321	0.3	0.3	95	14	1995.9-1999.6
P049	121.5808	25.1656	3.8	116	0.8	0.8	143	5	1993.2-1997.9
PKGM	120.3056	23.5800	7.7	327	0.2	0.2	95	17	1995.2-1999.6
S002	119.4386	23.2133	0.2	191	0.4	0.3	99	6	1993.4-1999.6
S003	120.1628	23.1731	2.5	252	0.4	0.3	108	11	1993.4-1999.0
S004	120.1886	23.3825	3.4	303	0.4	0.3	77	8	1993.4-1998.6
S005	120.2167	23.5992	2.4	80	0.5	0.4	79	7	1993.4-1998.6
S007	120.3831	23.2542	13.0	277	0.5	0.4	81	7	1993.4-1998.6
S008	120.4436	23.4200	11.3	287	0.5	0.5	79	7	1993.4-1998.6
S011	120.3394	23.2056	10.5	286	0.2	0.2	87	12	1993.4-1999.6
S012	120.4883	23.0594	33.2	270	0.2	0.2	97	12	1993.4-1999.6
S013	120.5636	23.2536	27.6	280	0.4	0.4	84	7	1993.4-1998.6
S014	120.6489	23.4044	22.7	273	0.4	0.4	92	8	1993.4-1998.6
S015	120.6814	23.5550	15.8	294	0.5	0.4	90	8	1993.4-1998.6
S016	120.8028	24.1794	9.2	286	0.3	0.2	79	8	1993.5-1999.6
S017	120.7644	24.6011	3.6	297	0.4	0.3	92	9	1993.5-1999.6
S018	121.0003	24.8833	2.6	228	0.3	0.3	87	9	1993.5-1999.6
S019	121.2914	25.1022	2.6	215	0.4	0.4	42	10	1993.2-1999.6
S01R	119.5925	23.6553	0.0	91	0.0	0.0	180	30	1993.2-1999.6
S020	121.5122	25.2853	2.5	201	0.4	0.4	84	8	1993.2-1998.9
S021	120.7131	21.9950	44.6	266	0.7	0.6	104	6	1993.4-1999.4
S022	120.6239	22.3664	48.6	268	0.5	0.4	87	7	1993.4-1999.4
S024	120.7036	22.9156	51.5	269	0.4	0.3	54	8	1993.4-1998.2
S025	120.8244	23.2636	30.8	275	0.5	0.5	83	7	1993.4-1998.5
S026	120.9164	23.2822	32.3	280	0.4	0.4	84	9	1993.4-1998.5
S027	120.8894	23.4839	28.2	282	0.3	0.3	85	15	1993.4-1999.4
S028	121.1425	23.7517	26.7	295	0.6	0.4	100	8	1994.2-1999.6
S029	121.5181	25.1272	2.0	165	0.4	0.4	95	7	1993.2-1998.9

S030	121.0275	24.2806	9.3	300	0.7	0.6	81	6	1993.5-1998.5
S031	121.3081	24.3378	10.0	321	0.3	0.3	82	10	1993.5-1999.6
S032	121.1139	24.5064	14.1	303	0.3	0.2	79	9	1993.5-1999.6
S033	121.2800	23.1031	63.5	312	0.5	0.4	84	7	1993.4-1999.4
S034	121.7742	24.8647	7.6	122	0.7	0.7	68	5	1996.3-1999.6
S035	121.9994	25.0056	4.8	156	0.3	0.3	72	10	1993.5-1999.6
S039	121.2758	23.2764	31.5	302	0.4	0.3	89	9	1993.4-1999.4
S040	121.1500	23.0306	33.5	292	0.4	0.4	85	8	1993.4-1999.4
S041	120.8489	21.9261	35.9	286	0.7	0.7	116	7	1993.4-1999.4
S042	120.8550	22.2419	42.4	281	0.5	0.4	98	10	1993.4-1999.4
S043	120.9350	22.4717	37.4	286	0.4	0.4	95	8	1993.4-1999.4
S044	121.0225	22.6778	31.2	281	0.4	0.4	92	11	1993.4-1999.4
S045	121.0806	22.8803	31.4	289	0.4	0.4	89	8	1993.4-1999.4
S046	121.0550	23.1472	31.3	292	0.4	0.4	87	8	1993.4-1999.4
S047	121.3594	23.4708	34.0	307	0.4	0.3	89	13	1993.4-1999.4
S048	121.4050	23.7094	24.6	299	0.3	0.3	82	14	1993.4-1999.6
S049	121.5406	23.8867	23.0	303	0.3	0.3	83	13	1993.4-1999.6
S050	121.6625	24.1453	7.8	278	0.3	0.3	88	12	1993.4-1999.6
S052	121.8678	24.5939	37.9	149	0.4	0.3	95	9	1994.9-1999.6
S053	121.7781	24.3972	22.9	140	0.4	0.4	105	9	1994.9-1999.6
S054	121.1975	22.7939	63.6	307	0.5	0.4	95	7	1993.4-1999.4
S055	121.1228	23.1342	32.1	293	0.6	0.5	90	7	1993.4-1999.4
S056	121.1986	23.0369	62.5	306	0.5	0.4	83	7	1993.4-1999.4
S057	121.3092	22.9731	65.8	309	0.4	0.4	90	7	1993.4-1999.4
S058	121.4544	23.3194	64.6	316	0.2	0.2	91	21	1993.4-1999.4
S059	121.5133	23.4883	66.3	315	0.5	0.5	79	7	1993.4-1999.4
S061	121.5589	23.7511	33.6	325	0.4	0.4	78	7	1993.4-1999.4
S064	120.5039	22.9486	47.1	270	0.6	0.5	88	9	1993.4-1998.0
S065	120.6111	23.1200	37.3	276	0.4	0.4	82	10	1993.4-1999.4
S066	120.5117	23.1922	29.9	277	0.6	0.5	79	7	1993.4-1998.5
S067	120.3839	22.9514	25.0	255	0.4	0.4	110	7	1993.4-1999.0
S068	120.3664	23.0853	10.8	254	0.8	0.7	126	5	1993.4-1999.0
S069	120.5011	23.3264	23.5	277	0.6	0.5	78	7	1993.4-1998.6
S070	120.5619	23.4519	16.1	282	0.4	0.4	82	9	1993.4-1998.6
S071	120.3219	23.4694	4.9	276	0.4	0.4	79	7	1993.4-1998.6
S072	121.1625	22.9256	63.7	305	0.5	0.4	79	7	1993.4-1999.4
S073	121.2881	23.2397	55.6	307	0.4	0.4	88	8	1993.4-1999.4

S074	121.4953	23.7158	34.5	322	0.4	0.3	77	8	1993.4-1999.4
S075	121.5283	23.8275	26.5	313	0.5	0.4	70	6	1993.4-1999.4
S077	121.5250	23.5964	62.0	317	0.5	0.4	71	7	1993.4-1999.4
S078	121.0453	23.1669	31.0	287	0.6	0.5	81	5	1993.4-1999.4
S079	121.0269	23.2011	29.1	281	0.9	0.8	69	5	1993.4-1998.3
S080	121.0131	23.2203	31.3	286	0.5	0.5	82	9	1993.4-1998.3
S082	120.3686	23.2353	11.3	275	1.4	1.1	61	6	1993.4-1998.5
S083	120.3892	23.2367	15.8	264	1.5	1.3	67	6	1993.4-1998.5
S085	120.4156	23.2356	15.6	259	1.1	0.9	72	6	1993.4-1998.5
S087	120.4486	23.2358	15.6	274	1.1	1.0	96	6	1993.4-1998.5
S088	120.4592	23.2403	20.2	279	1.0	0.9	85	6	1993.4-1998.5
S089	120.4675	23.2211	20.0	275	0.9	0.9	84	6	1993.4-1998.5
S090	120.4806	23.2094	24.5	269	0.9	0.9	87	6	1993.4-1998.5
S091	120.4942	23.2047	30.0	277	1.2	1.1	121	6	1993.4-1998.5
S092	120.5286	23.1850	29.9	279	0.4	0.3	107	11	1993.4-1999.6
S093	121.6267	24.0147	14.6	311	0.4	0.3	86	8	1993.4-1999.6
S094	120.5014	23.6606	5.4	307	0.4	0.3	80	11	1993.4-1998.6
S095	121.6511	25.2292	4.5	154	1.3	1.2	123	4	1996.3-1998.9
S096	120.3383	22.7703	45.6	258	1.7	1.6	119	5	1996.1-1999.6
S097	120.3864	22.7756	45.7	252	1.2	1.1	99	5	1996.1-1999.0
S098	121.4344	23.6242	44.9	305	1.1	1.1	94	4	1996.5-1999.4
S099	121.4914	23.6339	47.7	313	0.9	0.9	67	4	1996.5-1999.4
S100	121.5008	23.5808	58.2	316	2.5	2.2	99	3	1997.1-1999.4
S101	121.6139	25.0406	6.1	164	0.1	0.1	72	24	1993.2-1999.6
S103	120.4753	23.5644	7.7	290	0.2	0.1	93	23	1993.4-1999.4
S104	121.1894	22.8208	62.3	309	0.2	0.1	95	24	1993.4-1999.6
S105	121.1128	22.9517	33.2	292	0.2	0.2	90	21	1993.4-1999.6
S122	121.4028	23.5783	37.4	301	1.2	1.1	92	4	1996.5-1999.4
S124	121.5353	24.4981	10.1	69	0.9	0.8	112	4	1996.5-1999.6
S125	120.7525	22.4058	48.0	273	2.3	2.1	96	3	1997.1-1999.4
S130	120.7433	22.7444	51.0	275	1.7	1.6	96	5	1997.1-1999.4
S23R	120.6061	22.6450	51.3	270	0.1	0.1	103	28	1993.2-1999.6
S291	120.3125	23.3383	8.9	257	1.2	1.1	93	6	1995.3-1998.6
S411	121.4008	25.1172	1.6	200	0.4	0.4	87	8	1993.2-1998.9
S412	121.4575	25.0775	1.7	166	0.4	0.4	65	8	1993.2-1998.9
S413	121.5797	24.9719	3.1	119	0.3	0.3	74	12	1993.2-1999.6
SANT	121.4164	23.1250	66.5	311	0.4	0.4	90	8	1993.4-1999.4

STCS	120.4808	23.5358	10.8	278	0.5	0.5	72	7	1993.4-1998.6
TAIW	121.5367	25.0214	2.7	86	0.1	0.1	72	20	1993.2-1998.9
TAPN	121.6356	25.0231	5.9	110	0.3	0.3	84	14	1993.2-1999.6
TECS	120.6550	24.3564	5.0	284	0.4	0.3	87	8	1994.9-1999.6
TFLS	121.0500	24.6806	4.5	324	0.3	0.3	80	10	1993.5-1999.6
TMLM	121.0075	22.6161	32.2	285	0.2	0.2	102	19	1995.2-1999.6
WK5A	121.4458	25.0692	0.6	86	2.4	2.0	84	4	1994.3-1998.9
WNTS	120.5844	24.1381	4.8	276	0.3	0.2	82	9	1993.5-1999.6
YMSM	121.5742	25.1658	2.3	118	0.2	0.2	81	22	1994.1-1999.6

*Sites to the east of the LVF*

0135	121.3486	23.2908	55.8	317	0.5	0.4	78	8	1993.4-1999.4
0207	121.1475	22.8178	58.6	303	0.6	0.6	70	6	1993.4-1998.3
0241	121.3347	23.3361	52.0	310	0.9	0.9	45	6	1994.2-1999.4
0242	121.3250	23.2961	58.3	317	1.4	1.3	45	5	1995.2-1999.4
0283	121.2336	23.1178	64.1	311	0.6	0.6	75	6	1993.4-1998.3
1215	121.5869	23.8878	28.0	316	0.4	0.4	70	8	1993.4-1999.4
8152	121.4872	23.6453	48.3	316	1.5	1.2	82	5	1996.1-1999.4
S033	121.2800	23.1031	63.5	312	0.5	0.4	84	7	1993.4-1999.4
S054	121.1975	22.7939	63.6	307	0.5	0.4	95	7	1993.4-1999.4
S056	121.1986	23.0369	62.5	306	0.5	0.4	83	7	1993.4-1999.4
S057	121.3092	22.9731	65.8	309	0.4	0.4	90	7	1993.4-1999.4
S058	121.4544	23.3194	64.6	316	0.2	0.2	91	21	1993.4-1999.4
S059	121.5133	23.4883	66.3	315	0.5	0.5	79	7	1993.4-1999.4
S061	121.5589	23.7511	33.6	325	0.4	0.4	78	7	1993.4-1999.4
S063	121.4786	22.6647	79.6	305	0.4	0.4	97	8	1993.4-1999.4
S072	121.1625	22.9256	63.7	305	0.5	0.4	79	7	1993.4-1999.4
S073	121.2881	23.2397	55.6	307	0.4	0.4	88	8	1993.4-1999.4
S074	121.4953	23.7158	34.5	322	0.4	0.3	77	8	1993.4-1999.4
S075	121.5283	23.8275	26.5	313	0.5	0.4	70	6	1993.4-1999.4
S077	121.5250	23.5964	62.0	317	0.5	0.4	71	7	1993.4-1999.4
S098	121.4344	23.6242	44.9	305	1.1	1.1	94	4	1996.5-1999.4
S099	121.4914	23.6339	47.7	313	0.9	0.9	67	4	1996.5-1999.4
S100	121.5008	23.5808	58.2	316	2.5	2.2	99	3	1997.1-1999.4
S102	121.5581	22.0372	81.5	302	0.3	0.2	105	14	1993.2-1996.5
S104	121.1894	22.8208	62.3	309	0.2	0.1	95	24	1993.4-1999.6
SANT	121.4164	23.1250	66.5	311	0.4	0.4	90	8	1993.4-1999.4

621  $V$  is the station velocity;  $Azi$  is the azimuth of  $V$ ;  $a$ ,  $b$  are the semi-major and semi-minor axes for error

622 ellipse of  $V$ ;  $Azi_a$  is the azimuth of  $a$ ;  $n$  is number of survey.

623

ACCEPTED MANUSCRIPT